J. Fluid Mech. (2014), *vol.* 745, *pp.* 251–278.
doi:10.1017/jfm.2014.72

Nonlinear stability of gravitationally unstable, transient, diffusive boundary layers in porous media

N. Tilton and A. Riaz†

Department of Mechanical Engineering, University of Maryland, College Park, MD 20742, USA

(Received 25 November 2012; revised 30 December 2013; accepted 30 January 2014; first published online 19 March 2014)

The linear stability of transient diffusive boundary layers in porous media has been studied extensively for its applications to carbon dioxide sequestration. The onset of nonlinear convection, however, remains understudied because the transient base state invalidates the traditional stability methods that are used for autonomous systems. We demonstrate that the onset time of nonlinear convection, $t = t_{on}$, can be determined from an expansion that is two orders of magnitude faster than a direct numerical simulation. Using the expansion, we explore the sensitivity of t_{on} to the initial perturbation magnitude and wavelength, as well as the initial time at which a perturbation is initiated. We find that there is an optimal initial time and wavelength that minimize t_{on}, and we obtain analytical relationships for these parameters in terms of aquifer properties and initial perturbation magnitude. This importance of the initial perturbation time and magnitude is often overlooked in previous studies. To investigate perturbation evolution at late-times, $t > t_{on}$, we perform direct numerical simulations that reveal two unique features of transient diffusive boundary layers. First, when a boundary layer is perturbed with a single horizontal Fourier mode, nonlinear mechanisms generate a zero-wavenumber response whose magnitude eventually surpasses that of the fundamental mode. Second, when a boundary layer is simultaneously perturbed with many Fourier modes, the late-time perturbation magnitude is concentrated in the zero-wavenumber mode, and there is no clearly dominant, non-zero, wavenumber. These unique results are further interpreted by comparison with direct numerical simulations of Rayleigh–Bénard convection.

Key words: buoyancy-driven instability, fingering instability, nonlinear instability

1. Introduction

This study is motivated by carbon dioxide sequestration in subsurface, porous, brine-saturated aquifers (Orr 2009). Following injection into an aquifer, buoyant CO_2 forms a horizontal layer of gas bounded by impermeable caprock above and brine below, as illustrated in figure 1(*a*). With time, CO_2 dissolves into the brine and forms a downwardly growing diffusive boundary layer. Because the brine density increases with dissolution of CO_2, a gravitational instability leads to the formation of finger-like structures that convect aqueous CO_2 downwards (Ennis-King & Paterson 2003). Predicting the onset of this convection is important for CO_2 sequestration as well as

† Email address for correspondence: ariaz@umd.edu

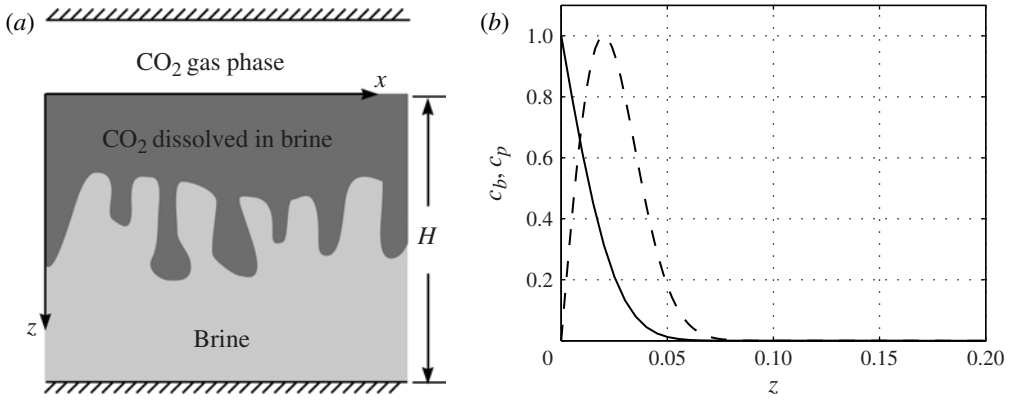

FIGURE 1. (*a*) Sketch (not to scale) of the geometry considered in the current study. Here CO_2 gas forms a layer beneath the impermeable caprock. At time $t = 0$, CO_2 begins dissolving into the underlying brine. Gravitational instability leads to the formation of fingers. (*b*) The transient base state (2.3) for $Ra = 500$ and $t = 0.1$ (solid line). The dashed line shows the corresponding initial perturbation (2.6), normalized so its maximum is unity, for $t_p = 0.1$. To ease visualization, c_b and c_p are shown for $0 \leqslant z \leqslant 0.2$ because both decay to zero well before $z = 1$.

heat transfer devices (Goldstein 1959) and geophysical flows (Green & Foster 1975; Wooding, Tylers & White 1997).

The linear stability of transient diffusive boundary layers has been studied extensively and is relatively well understood (Rees, Selim & Ennis-King 2008). During the initial formation of the boundary layer, perturbations are strongly damped. Eventually, a critical time for linear instability, $t = t_c$, is reached after which perturbations grow. Numerical simulations show that linear mechanisms can dominate for considerable time beyond t_c (Riaz *et al.* 2006; Rapaka *et al.* 2008; Daniel, Tilton & Riaz 2013; Tilton, Daniel & Riaz 2013). Within this linear regime, the horizontal wavenumber, k, and growth rate of the dominant perturbations vary significantly with time. The linear stability of these perturbations has been studied using both quasi-steady methods (Morton 1957; Goldstein 1959; Lick 1965; Robinson 1976) and by solving the linear initial value problem (IVP). The initial condition for the IVP may be prescribed arbitrarily (Foster 1965; Gresho & Sani 1971; Caltagirone 1980; Kaviany 1984; Ennis-King & Paterson 2003), set to the dominant eigenmode of the diffusion operator in self-similar space (Riaz *et al.* 2006), or determined from an optimization procedure (Rapaka *et al.* 2008; Doumenc *et al.* 2010; Slim & Ramakrishnan 2010). Recently, Daniel *et al.* (2013) determined optimal perturbations that support finite amplitudes and found them to be consistent with the dominant mode initial condition of Riaz *et al.* (2006).

The current study is concerned with perturbation evolution after the critical time for linear instability, $t > t_c$. This includes the initial regime of linear instability, and the ensuing nonlinear regime when nonlinear mechanisms cause perturbations to deviate from linear theory. This onset of nonlinear convection is of considerable importance because it is the primary mechanism for dissolution of CO_2 into brine (Ennis-King & Paterson 2003). Within the linear regime, the net dissolution flux, J, of CO_2 decreases with time. The onset of nonlinear convection, however, initiates a period of accelerated dissolution. Consistent with experimental (Blair & Quinn 1969) and numerical (Jhaveri

& Homsy 1982; Rapaka *et al.* 2008; Daniel *et al.* 2013; Tilton *et al.* 2013) studies, we define the *onset time of nonlinear convection*, t_{on}, as the time at which $\mathrm{d}J/\mathrm{d}t = 0$. A major goal of the current study is to develop an efficient method of determining t_{on} without resorting to direct numerical simulations (DNS). Using such a method, we then wish to produce simple relationships for t_{on} in terms of aquifer properties. Such relationships have been lacking to date, and they constitute a major step forward from linear analyses concerned mostly with the critical time for linear instability, t_c.

The nonlinear stability of transient diffusive boundary layers remains understudied. To understand why, it is helpful to consider Rayleigh–Bénard (RB) convection in a fluid layer heated from below. In this case, the base state is steady and a traditional eigenmode analysis produces a critical Rayleigh number, Ra_c, and horizontal wavenumber, k_c, for the equilibrium state of the dominant perturbation. For weakly supercritical Rayleigh numbers, $0 < Ra - Ra_c \ll 1$, the perturbation growth rates are small and nonlinear stability analyses can expand the flow fields about the equilibrium state using a multiple-scale expansion (Godreche & Manneville 1998) of the form

$$\theta(\boldsymbol{x}, t) = \epsilon\theta_1(\boldsymbol{x}, \tau_0, \tau_1, \tau_2, \ldots) + \epsilon^2\theta_2(\boldsymbol{x}, \tau_0, \tau_1, \tau_2, \ldots) + \epsilon^3\theta_3(\boldsymbol{x}, \tau_0, \tau_1, \tau_2, \ldots) + \cdots \tag{1.1}$$

where θ is the perturbation temperature field, $\epsilon \ll 1$ is a small parameter and $\tau_j = \epsilon^j t$ are multiple time scales over which nonlinear mechanisms occur. In comparison with RB convection, the nonlinear stability of transient diffusive boundary layers is complicated by the transient base state. This has three main consequences. First, the eigenmode approach is invalid. Second, there is no equilibrium state about which to perform an expansion of type (1.1). Third, the separation of temporal variations into distinct time scales, τ_j, is unclear because the growth rates of the base state and perturbations vary significantly with time and are not generally small (Riaz *et al.* 2006; Tilton *et al.* 2013). Consequently, the second goal of the current study is to study nonlinear convection through DNS to determine whether transient diffusive boundary layers are amenable to weakly nonlinear expansions of form (1.1).

Despite the above-noted difficulties, Robinson (1976) attempted to investigate the weakly nonlinear stability of transient diffusive boundary layers in porous media using a quasi-steady approach. Robinson noted that this approach provides only qualitative results because it is based on mutually exclusive assumptions. The quasi-steady assumption requires perturbations have a large growth rate, while Robinson's asymptotic expansion requires perturbations have a small growth rate. Subsequently, the onset time of nonlinear thermal convection in fluid layers was investigated by Jhaveri & Homsy (1982) using a two-dimensional nonlinear IVP method that considers nonlinear interactions between a fundamental wavenumber and a zero-wavenumber response. This produces quantitative results that agree with experimental results for t_{on}. However, because the nonlinear IVP depends on the initial perturbation magnitude, and because the dominant wavenumbers vary temporally, the nonlinear IVP must be solved numerically for many potential dominant wavenumbers and initial perturbation magnitudes.

The current study investigates the onset of nonlinear convection using three complementary methodologies. We first investigate the onset time of nonlinear convection, t_{on}, by performing a regular asymptotic expansion about the transient base state. We then investigate the subsequent perturbation evolution for $t > t_{on}$ using high-order DNS and the nonlinear IVP of Jhaveri & Homsy (1982). The regular asymptotic expansion avoids the quasi-steady assumption of Robinson (1976) and is approximately one order of magnitude faster than the nonlinear IVP of Jhaveri

& Homsy (1982) and two orders of magnitude faster than DNS. The speedup occurs because the expansion produces linear partial differential equations that are independent of the initial perturbation magnitude. Consequently, the expansion can be solved once for a given perturbation structure, and the initial perturbation magnitude can then be varied independently to observe its effect on t_{on}. The efficiency of the expansion makes it computationally feasible for us to perform a thorough parametric study of t_{on} in terms of the perturbation wavenumber, k, initial perturbation magnitude, ϵ, initial perturbation time, t_p, and Rayleigh number, Ra.

The current study makes four main contributions. (i) We show that the regular asymptotic expansion accurately determines t_{on} to within 1 % of DNS. Although beyond the scope of the current study, the expansion can be extended to anisotropic aquifers with vertical heterogeneity, and can also be coupled with the procedure of Daniel *et al.* (2013) to investigate optimal perturbation structures. (ii) We show that when the boundary layer is perturbed with a single Fourier mode at an initial time t_p, there is an optimal initial time and wavenumber that minimize the onset time of nonlinear convection. Furthermore, onset occurs when perturbations attain a critical magnitude. By rescaling the problem, we find analytical relationships for these optimal parameters in terms of aquifer properties and the initial perturbation magnitude. Such relationships have been lacking to date, and show the importance of the initial perturbation time and magnitude, which are often overlooked in previous studies. (iii) Using DNS, we demonstrate that when the boundary layer is perturbed with a single Fourier mode, nonlinear mechanisms generate a zero-wavenumber response whose magnitude becomes equal order with the fundamental mode after $t = t_{on}$. This indicates that any weakly nonlinear expansion that assumes the zero-wavenumber response is small compared with the fundamental mode will likely fail after $t = t_{on}$. The nonlinear IVP of Jhaveri & Homsy (1982), however, shows excellent agreement with DNS for the late times, $t > t_{on}$, because it assumes the zero-wavenumber response to be equal order with the fundamental mode. (iv) Finally, we consider boundary layers that are simultaneously perturbed with many Fourier modes. We demonstrate that such systems have an initial linear regime, $t \leqslant t_{on}$, during which nonlinear interactions between simultaneously perturbed modes may be neglected. Consequently, the total flux at the onset of convection is well approximated by a linear combination of fluxes associated with each perturbed mode. For $t > t_{on}$, however, these systems are dominated by strongly nonlinear interactions between perturbed modes, and cannot be studied using weakly nonlinear expansions or the method of Jhaveri & Homsy (1982).

This study is organized in the following manner. We present the governing equations in § 2, and the methodology in § 3. In § 4, we explore the onset time of nonlinear convection using the regular asymptotic expansion. In § 5, we explore perturbation evolution for the late times, $t > t_{on}$. We summarize our conclusions in § 6. The DNS method is benchmarked in appendix A. Corresponding results for weakly supercritical RB convection are provided in appendix B.

2. Governing equations and stability problem

We consider a homogeneous, isotropic, brine-saturated porous region delimited by a layer of CO_2 gas at $z = 0$ and a layer of impermeable rock at $z = H$, as illustrated in figure 1(*a*). The domain is of infinite horizontal extent and the z-axis points downward in the direction of gravity. The porous medium has a permeability K, dispersion coefficient $\mathscr{D}$ and porosity ϕ. The brine is initially quiescent with zero CO_2 concentration, $c = 0$, and uniform density $\rho = \rho_0$. Following most previous

work, we model CO_2 dissolution by assuming that at time $t = 0$, saturated brine is supplied at $z = 0$ with a constant concentration $c = C_1$ and density $\rho = \rho_1$. Note that $\rho_1 > \rho_0$ because the brine density increases with the dissolution of CO_2 (Ennis-King & Paterson 2003). The fluid viscosity, μ, is assumed constant. To be consistent with previous numerical studies (Riaz *et al.* 2006; Rapaka *et al.* 2008; Pau *et al.* 2010; Daniel *et al.* 2013; Hewitt, Neufeld & Lister 2013) and two-dimensional Hele–Shaw experiments (Green & Foster 1975; Slim *et al.* 2013), we consider two-dimensional convection in the x–z plane. We also note that the previous two-dimensional analysis of Jhaveri & Homsy (1982) showed excellent agreement with three-dimensional experimental results for onset of thermal convection in fluid layers.

We model advection–diffusion using volume-averaged forms of the advection–diffusion, Darcy and continuity equations (Whitaker 1999). Because the density difference $\Delta\rho = \rho_1 - \rho_0$ is typically of the order of 1 % (Ennis-King & Paterson 2003), we use the Boussinesq approximation with the linear density profile $\rho = \rho_0 + \Delta\rho(c/C_1)$. Following the standard procedure (Riaz *et al.* 2006), the governing equations and boundary conditions may be expressed as

$$\frac{\partial c}{\partial t} + u\frac{\partial c}{\partial x} + w\frac{\partial c}{\partial z} - \frac{1}{Ra}\nabla^2 c = 0, \quad \nabla^2 w - \frac{\partial^2 c}{\partial x^2} = 0, \quad \frac{\partial u}{\partial x} + \frac{\partial w}{\partial z} = 0, \tag{2.1}$$

$$c\Big|_{z=0} = 1, \quad \frac{\partial c}{\partial z}\Big|_{z=1} = 0, \quad w\Big|_{z=0} = w\Big|_{z=1} = 0, \tag{2.2}$$

where u and w are the horizontal and vertical fluid velocities, respectively. Equations (2.1) and (2.2) are non-dimensionalized as in Riaz *et al.* (2006) using the characteristic length H, buoyancy velocity $U = K\Delta\rho g/\mu$, time $\phi H/U$ and concentration C_1. The Rayleigh number is defined as $Ra = UH/\phi\mathscr{D}$.

Note from (2.2) that the velocity field produced by Darcy's law does not satisfy the no-slip condition. The issue of how to model fluid flow at an interface between a porous medium and an impermeable wall remains an open problem. This is because the assumptions of homogeneity and isotropy are invalid in a thin layer adjacent to the lower wall where the porosity and permeability vary rapidly (Whitaker 1986). Currently, there are two main approaches to modelling impermeable boundaries. The first adds a viscous Laplacian term to Darcy's law that allows the application of a no-slip condition (Sparrow *et al.* 1973; Hirata, Goyeau & Gobin 2007; Tilton & Cortelezzi 2008) or a zero tangential stress (Camporeale, Mantelli & Manes 2013). This has been criticized because it violates the length-scale constraints of Darcy's law (Whitaker 1986). The second approach, overwhelmingly used in studies of CO_2 sequestration, uses the traditional form of Darcy's law and applies only the no-penetration condition. Both approaches are engineering approximations. We choose the second approach because there is some numerical evidence that suggests the no-slip assumption has a negligible effect on the volume-averaged flow fields (James & Davis 2001; Breugem & Boersma 2005). We also show in § 4.3 that the end-effects at $z = 1$ play no role in determining the onset time of nonlinear convection, t_{on}.

Equations (2.1) and (2.2) admit the transient base state,

$$\boldsymbol{v}_b = 0, \quad c_b(z,t) = 1 - \frac{4}{\pi}\sum_{n=1}^{\infty}\frac{1}{2n-1}\sin\left[\left(n-\frac{1}{2}\right)\pi z\right]\exp\left[-\left(n-\frac{1}{2}\right)^2\frac{\pi^2 t}{Ra}\right]. \tag{2.3}$$

Figure 1(*b*) illustrates c_b (solid line) for $Ra = 500$ and $t = 0.1$. We investigate onset of nonlinear convection by solving (2.1) and (2.2) subject to an initial condition that is the sum of base state (2.3) and a small, spatially periodic, perturbation originating at time $t = t_p$,

$$\begin{bmatrix} c \\ u \\ w \end{bmatrix}_{t=t_p} = \begin{bmatrix} c_b(z, t_p) \\ 0 \\ 0 \end{bmatrix} + \epsilon \begin{bmatrix} c_p(z)(\mathrm{e}^{\mathrm{i}kx} + \mathrm{e}^{-\mathrm{i}kx}) \\ \mathrm{i}u_p(z)(\mathrm{e}^{\mathrm{i}kx} - \mathrm{e}^{-\mathrm{i}kx}) \\ w_p(z)(\mathrm{e}^{\mathrm{i}kx} + \mathrm{e}^{-\mathrm{i}kx}) \end{bmatrix}, \tag{2.4}$$

where $c_p(z)$, $w_p(z)$ and $u_p(z) = (1/k)(\mathrm{d}w_p/\mathrm{d}z)$ are real-valued shape functions, k is the horizontal wavenumber and $i = \sqrt{-1}$. The perturbation satisfies (2.1) and (2.2), and is scaled so the initial perturbation amplitude, measured using a root-mean-square average over the horizontal wavelength $\lambda = 2\pi/k$, satisfies

$$\left\{ \frac{1}{\lambda} \int_0^{\lambda} \int_0^1 \frac{1}{2} [u^2 + w^2 + (c - c_b)^2]_{t=t_p} \mathrm{d}z \, \mathrm{d}x \right\}^{1/2} = \epsilon, \tag{2.5}$$

where $\epsilon \ll 1$ is the initial perturbation amplitude. In practice, we prescribe c_p, and u_p and w_p are determined from (2.1). Note that for a given c_p, Ra and t_p, there is a maximum initial amplitude, ϵ_{max}, above which initial condition (2.4) produces unphysical regions of negative concentration (Daniel *et al.* 2013).

Experimentally, perturbations are observed to originate within the boundary layer (Spangenberg & Rowland 1961; Blair & Quinn 1969). For this reason, we consider the following popular initial perturbation that is concentrated within the boundary layer (Ben, Demekhin & Chang 2002; Pritchard 2004; Riaz *et al.* 2006; Elenius, Nordbotten & Kalisch 2012; Kim & Choi 2012)

$$c_p = \xi \mathrm{e}^{-\xi^2}, \quad \xi = z\sqrt{Ra/(4\,t_p)}. \tag{2.6}$$

The dashed line in figure 1(*b*) illustrates initial perturbation (2.6) for $Ra = 500$ and $t_p = 0.1$. Perturbation (2.6) decays rapidly to zero outside the boundary layer so that $c_p < 10^{-20}$ when $z = 0.2$. Consequently, figure 1(*b*) only shows results for $z \leqslant 0.2$. The popularity of (2.6) arises from studies that approximate the aquifer depth as semi-infinite for small times when the end-effects at $z = 1$ are negligible (Riaz *et al.* 2006). It is applicable to finite-depth systems provided that $\sqrt{4t_p/Ra} \ll 1$ (Riaz *et al.* 2006). We use initial condition (2.6) due to its popularity and because Daniel *et al.* (2013) have shown that it is consistent with experiments and optimal perturbations in systems of finite depth, H.

The stability of a transient boundary layer is sensitive to the initial time, $t = t_p$, at which it is perturbed. In the current study, we first consider perturbations originating near $t_p = 0$, as is common practice in previous studies. We then vary t_p to find the optimal initial perturbation time that minimizes the onset time for nonlinear convection.

3. Methodology

3.1. *Asymptotic expansion*

We exploit the small initial perturbation amplitude, ϵ, to seek a solution to (2.1)–(2.4) in the form of a regular asymptotic expansion about the transient base state,

$$\begin{bmatrix} c \\ u \\ w \end{bmatrix} \approx \begin{bmatrix} c_b(z, t) \\ 0 \\ 0 \end{bmatrix} + \epsilon \begin{bmatrix} c_1(\boldsymbol{x}, t) \\ u_1(\boldsymbol{x}, t) \\ w_1(\boldsymbol{x}, t) \end{bmatrix} + \epsilon^2 \begin{bmatrix} c_2(\boldsymbol{x}, t) \\ u_2(\boldsymbol{x}, t) \\ w_2(\boldsymbol{x}, t) \end{bmatrix}. \tag{3.1}$$

We use the term 'regular' asymptotic expansion to differentiate expansion (3.1) from Lindstedt–Poincaré and multiple-scale expansions (Nayfeh 1981). Expansions of type (3.1) are also referred to as 'straightforward' by Nayfeh (1981). Expansion (3.1) assumes the second-order flow field, $\epsilon^2[c_2\ u_2\ w_2]^{\mathrm{T}}$, is small compared with the first-order field, $\epsilon[c_1\ u_1\ w_1]^{\mathrm{T}}$, which is small compared with c_b, which is of order unity. Substituting (3.1) into (2.1)–(2.4) and collecting orders of ϵ yields a hierarchy of linear IVPs. At first order in ϵ, we obtain

$$\frac{\partial c_1}{\partial t} + w_1\frac{\partial c_b}{\partial z} - \frac{1}{Ra}\nabla^2 c_1 = 0, \quad \nabla^2 w_1 = \frac{\partial^2 c_1}{\partial x^2}, \quad \frac{\partial u_1}{\partial x} = -\frac{\partial w_1}{\partial z}, \tag{3.2}$$

$$c_1\Big|_{z=0} = \frac{\partial c_1}{\partial z}\Big|_{z=1} = w_1\Big|_{z=0} = w_1\Big|_{z=1} = 0, \quad c_1\Big|_{t=t_p} = c_p(z)\left(\mathrm{e}^{\mathrm{i}kx} + \mathrm{e}^{-\mathrm{i}kx}\right), \tag{3.3}$$

to which we find the solution

$$\begin{bmatrix} c_1 \\ u_1 \\ w_1 \end{bmatrix} = \begin{bmatrix} \widehat{c}_1(z,t)\left(\mathrm{e}^{\mathrm{i}kx} + \mathrm{e}^{-\mathrm{i}kx}\right) \\ \mathrm{i}\widehat{u}_1(z,t)\left(\mathrm{e}^{\mathrm{i}kx} - \mathrm{e}^{-\mathrm{i}kx}\right) \\ \widehat{w}_1(z,t)\left(\mathrm{e}^{\mathrm{i}kx} + \mathrm{e}^{-\mathrm{i}kx}\right) \end{bmatrix}, \tag{3.4}$$

$$\frac{\partial \widehat{c}_1}{\partial t} + \widehat{w}_1\frac{\partial c_b}{\partial z} - \frac{1}{Ra}\left(\frac{\partial^2}{\partial z^2} - k^2\right)\widehat{c}_1 = 0, \quad \left(\frac{\partial^2}{\partial z^2} - k^2\right)\widehat{w}_1 = -k^2\widehat{c}_1, \quad \widehat{u}_1 = \frac{1}{k}\frac{\partial \widehat{w}_1}{\partial z}, \tag{3.5}$$

$$\widehat{c}_1\Big|_{z=0} = \frac{\partial \widehat{c}_1}{\partial z}\Big|_{z=1} = \widehat{w}_1\Big|_{z=0} = \widehat{w}_1\Big|_{z=1} = 0, \quad \widehat{c}_1\Big|_{t=t_p} = c_p(z). \tag{3.6}$$

Hereinafter, we use the $\widehat{\ }$ symbol to denote functions dependent on z and t only.

At second order in ϵ, we obtain the following forced, linear IVP

$$\frac{\partial c_2}{\partial t} + w_2\frac{\partial c_b}{\partial z} - \frac{1}{Ra}\nabla^2 c_2 = f_2, \quad \nabla^2 w_2 = \frac{\partial^2 c_2}{\partial x^2}, \quad \frac{\partial u_2}{\partial x} = -\frac{\partial w_2}{\partial z}, \tag{3.7}$$

$$c_2\Big|_{z=0} = \frac{\partial c_2}{\partial z}\Big|_{z=1} = w_2\Big|_{z=0} = w_2\Big|_{z=1} = 0, \quad c_2\Big|_{t=t_p} = 0, \tag{3.8}$$

where $f_2 = -\boldsymbol{v}_1 \cdot \nabla c_1$ arises due to nonlinear interactions of the fundamental disturbance

$$f_2 = -2\frac{\partial}{\partial z}\left(\widehat{c}_1\widehat{w}_1\right) - \left(\widehat{w}_1\frac{\partial \widehat{c}_1}{\partial z} - \widehat{c}_1\frac{\partial \widehat{w}_1}{\partial z}\right)\left(\mathrm{e}^{\mathrm{i}2kx} + \mathrm{e}^{-\mathrm{i}2kx}\right). \tag{3.9}$$

The first term on the right-hand-side of (3.9) does not vary horizontally, while the second term varies sinusoidally with a horizontal wavenumber $2k$. We exploit the linearity of (3.7)–(3.9) to find a solution as the sum of two responses to the forcing at the zero wavenumber and second harmonic,

$$\begin{bmatrix} c_2 \\ u_2 \\ w_2 \end{bmatrix} = \begin{bmatrix} \widehat{c}_2^{(0)}(z,t) \\ 0 \\ 0 \end{bmatrix} + \begin{bmatrix} \widehat{c}_2^{(2)}(z,t)\left(\mathrm{e}^{\mathrm{i}2kx} + \mathrm{e}^{-\mathrm{i}2kx}\right) \\ \mathrm{i}\widehat{u}_2^{(2)}(z,t)\left(\mathrm{e}^{\mathrm{i}2kx} - \mathrm{e}^{-\mathrm{i}2kx}\right) \\ \widehat{w}_2^{(2)}(z,t)\left(\mathrm{e}^{\mathrm{i}2kx} + \mathrm{e}^{-\mathrm{i}2kx}\right) \end{bmatrix}, \tag{3.10}$$

where the superscript denotes the index of the harmonic component. The zero-wavenumber response, $\widehat{c}_2^{(0)}$, represents a nonlinear modification of the vertical mean concentration profile. The zero-wavenumber and second-harmonic responses satisfy

$$\frac{\partial \widehat{c}_2^{(0)}}{\partial t} - \frac{1}{Ra}\frac{\partial^2 \widehat{c}_2^{(0)}}{\partial z^2} = -2\frac{\partial}{\partial z}(\widehat{c}_1\widehat{w}_1), \tag{3.11}$$

$$\left(\frac{\partial^2}{\partial z^2} - 4k^2\right)\widehat{w}_2^{(2)} = -4k^2\widehat{c}_2^{(2)}, \quad \widehat{u}_2^{(2)} = \frac{1}{2k}\frac{\partial \widehat{w}_2^{(2)}}{\partial z}, \tag{3.12}$$

$$\frac{\partial \widehat{c}_2^{(2)}}{\partial t} + \widehat{w}_2^{(2)}\frac{\partial c_b}{\partial z} - \frac{1}{Ra}\left(\frac{\partial^2}{\partial z^2} - 4k^2\right)\widehat{c}_2^{(2)} = -\left(\widehat{w}_1\frac{\partial \widehat{c}_1}{\partial z} - \widehat{c}_1\frac{\partial \widehat{w}_1}{\partial z}\right), \tag{3.13}$$

where $\widehat{c}_2^{(0)}$, $\widehat{c}_2^{(2)}$, $\widehat{w}_2^{(0)}$ and $\widehat{w}_2^{(2)}$, satisfy the boundary and initial conditions (3.8). Equations (3.5), (3.6) and (3.11)–(3.13) are solved numerically using standard Chebyshev collocation methods with a third-order temporal discretization (Peyret 2002).

From (3.5) and (3.6), we note that the first-order IVP evolves independently of the higher-order problems. Consequently, expansion (3.1) cannot account for the nonlinear saturation of the fundamental mode, and we expect the expansion to eventually break down due to the growth of secular terms (Nayfeh 1981). Prior to breaking down, however, expansion (3.1) accurately predicts the onset time t_{on}. Our motivations for not pursuing a multiple-scale expansion are made clear in § 5.2 where we demonstrate that such an expansion may not be relevant to physical systems in which many Fourier modes are simultaneously perturbed. Furthermore, the regular asymptotic expansion (3.1) is particularly efficient computationally. This allows us to perform a thorough parametric study of the onset time t_{on} in terms of k, Ra, t_p and ϵ.

3.2. *High-order, pseudospectral, DNS*

We compare expansion (3.1) with DNS of equations (2.1)–(2.4), discretized temporally using the following third-order scheme (Peyret 2002),

$$\frac{11c^{n+1} - 18c^n + 9c^{n-1} - 2c^{n-2}}{6\delta t} + 3\mathrm{NL}^n - 3\mathrm{NL}^{n-1} + \mathrm{NL}^{n-2} = \frac{1}{Ra}\nabla^2 c^{n+1}, \tag{3.14}$$

$$\nabla^2 w^{n+1} = \frac{\partial^2 c^{n+1}}{\partial x^2}, \quad \frac{\partial u^{n+1}}{\partial x} = -\frac{\partial w^{n+1}}{\partial z}, \tag{3.15}$$

$$w^{n+1}\Big|_{z=0} = w^{n+1}\Big|_{z=1} = 0, \quad c^{n+1}\Big|_{z=0} = 1, \quad \frac{\partial c^{n+1}}{\partial z}\Big|_{z=1} = 0, \tag{3.16}$$

where $\mathrm{NL}^n = u^n\partial c^n/\partial x + w^n\partial c^n/\partial z$. The horizontal domain is truncated to $x \in [0, L]$ with periodic boundary conditions at $x = 0$ and $x = L$. We map $(x, z) \in [0, L] \times [0, 1]$ to $[x^*, z^*] = [0, 2\pi] \times [-1, 1]$ and approximate c^n and $\boldsymbol{v}^n$ as

$$f^n(x^*, z^*) \approx \sum_{l=-N_x/2}^{N_x/2-1}\sum_{m=0}^{N_z} a_{lm}\, \mathrm{e}^{\mathrm{i}lx^*} T_m(z^*), \tag{3.17}$$

where $f^n = (c^n, \boldsymbol{v}^n)$, a_{lm} are expansion coefficients, and T_m is the Chebyshev polynomial of order m. Note that N_x is always taken to be even because this facilitates our fast Fourier transform (FFT) routines. In the computation of the nonlinear terms NL^n,

aliasing is removed using the '3/2 rule' (Peyret 2002). For all simulations, we set $L = 2\pi$ to resolve integer wavenumbers, k. Spatial resolution is verified by ensuring the spectral coefficients decay to numerical precision. Temporal resolution is verified by ensuring the results are independent of δt. The numerical accuracy of the DNS scheme is verified in appendix A.

3.3. *Measures of perturbation growth and solute flux*

We measure the magnitude of each horizontal Fourier mode of the DNS perturbation flow fields with respect to the following norm,

$$E_l(t) = \left[\frac{1}{\lambda_l}\int_0^{\lambda_l}\int_0^1 \frac{1}{2}\left(\widetilde{u}_l^2 + \widetilde{w}_l^2 + \widetilde{c}_l^2\right) \mathrm{d}z\,\mathrm{d}x\right]^{1/2}, \tag{3.18}$$

where $\widetilde{u}_l$, $\widetilde{w}_l$ and $\widetilde{c}_l$ are the perturbation velocity and concentration fields generated by the Fourier modes with wavenumbers l and $-l$, where $l \geqslant 0$, and $\lambda_l = 2\pi/l$ is the mode's wavelength. When $l = 0$, E_0 is computed by setting $\lambda_0 = 1$. The perturbation concentration field is computed by subtracting the base state from the total DNS concentration field, $\widetilde{c} = c - c_b$. The Fourier components $\widetilde{c}_l$ are then computed using classical FFT routines. The perturbation magnitude (3.18) includes both the velocity and concentration perturbation fields, and is identical to the norms used by Doumenc *et al.* (2010) and Daniel *et al.* (2013). Our definition of E_l may be interpreted as a 'generalized energy' in the sense described by Joseph (1976), and is consistent with our definition of the initial magnitude ϵ. Note that the symbol k always refers to the wavenumber of the fundamental mode that is perturbed at $t = t_p$ through initial condition (2.4). Substituting expansion (3.1) in the norm (3.18), one finds that the magnitudes of the fundamental mode, E_k, zero-wavenumber mode, E_0, and second-harmonic mode, E_{2k}, can be computed from the expansion through the relations

$$E_k = \epsilon\left[\int_0^1 (\widehat{u}_1^2 + \widehat{w}_1^2 + \widehat{c}_1^2)\,\mathrm{d}z\right]^{1/2}, \quad E_0 = \epsilon^2\left[\int_0^1 (\widehat{c}_2^{(0)})^2\,\mathrm{d}z\right]^{1/2}, \tag{3.19}$$

$$E_{2k} = \epsilon^2\left\{\int_0^1 [(\widehat{u}_2^{(2)})^2 + (\widehat{w}_2^{(2)})^2 + (\widehat{c}_2^{(2)})^2]\,\mathrm{d}z\right\}^{1/2}. \tag{3.20}$$

We measure the solute flux across the gas interface at $z = 0$ with respect to an average over the fundamental wavelength $\lambda_k = 2\pi/k$,

$$J(t) = \frac{1}{\lambda_k}\int_0^{\lambda_k} \frac{1}{Ra}\left.\frac{\partial c}{\partial z}\right|_{z=0} \mathrm{d}x. \tag{3.21}$$

We also measure the portion of the flux due to the base state as

$$J_b(t) = \left.\frac{1}{Ra}\frac{\partial c_b}{\partial z}\right|_{z=0}. \tag{3.22}$$

4. The onset of nonlinear convection

This section explores the onset time of nonlinear convection using expansion (3.1). In § 4.1, we validate expansion (3.1) with comparison to DNS for a fixed Rayleigh number, Ra, and initial time, t_p. In § 4.2, we demonstrate that onset of nonlinear convection occurs when perturbations attain a critical magnitude. In § 4.3, we demonstrate that for a given Rayleigh number, Ra, and initial perturbation magnitude, ϵ, there is an optimal initial time and wavenumber that minimize the onset time of nonlinear convection.

4.1. *The onset time of nonlinear convection for fixed Ra and t_p*

In this section, we explore onset of nonlinear convection for the fixed Rayleigh number $Ra = 500$, which is typical of CO_2 sequestration (Ennis-King & Paterson 2003), and for the fixed initial time $t_p = 0.01$. The initial time is set one order of magnitude smaller than the critical time for linear instability, t_c. The critical time is defined as the time for which $\mathrm{d}E_k(t_c)/\mathrm{d}t = 0$, after which perturbations begin to grow. There is no unique value of t_c because it depends on k, Ra, t_p and c_p. However, studies show that $t_c \sim \mathscr{O}(0.1)$ for $Ra = 500$ (Ennis-King & Paterson 2003; Riaz *et al.* 2006; Slim & Ramakrishnan 2010).

The solid lines in figure 2(*a*) illustrate DNS results for the flux, J, when $k = 30$ and $\epsilon = 10^{-3}$, 10^{-4}, 10^{-5} and 10^{-6}. For $k = 30$, the perturbations are damped up to the time $t_c = 0.219$, after which linear instability causes the perturbation magnitudes to increase. The initial damped period, $t < 0.219$, is shaded grey in figure 2(*a*). The DNS results for J equal that due to the base state, J_b (dashed line) for considerable time after $t_c = 0.219$. Eventually, nonlinear effects cause DNS results to deviate from J_b such that each solid line has two turning points. The first turning point marks the onset time, t_{on}, at which J begins increasing. The increase occurs due to the nonlinear zero-wavenumber response that increases the concentration gradient at the gas interface, $z = 0$, see (3.21). The second turning point marks the time at which J attains a local maximum and begins decreasing. With increasing initial amplitude, ϵ, the duration of the linear regime decreases, and the maximum flux at the second turning point increases. For comparison, the dash-dotted lines demonstrate the flux predicted by expansion (3.1), which accurately predicts the duration of the linear regime and the onset of nonlinear convection. For $\epsilon = 10^{-3}$, expansion (3.1) predicts $t_{on} = 2.606$ compared with $t_{on} = 2.629$ predicted by DNS; a difference of less than 1 %. Following onset of convection, however, expansion (3.1) overpredicts J. The overprediction occurs due to the breakdown of expansion (3.1) from secular terms that grow without bound (Nayfeh 1981). These terms appear because expansion (3.1) does not account for slow nonlinear variations occurring over long time scales. Taking expansion (3.1) to third order, $\mathscr{O}(\epsilon^3)$, neither improves the results for t_{on} nor prevents breakdown. This will be discussed in greater detail in § 5.1.

We compute t_{on} for the integer wavenumbers $6 \leqslant k \leqslant 40$ and $\epsilon = 10^{-3}, 10^{-4}, 10^{-5}$ and 10^{-6}. Figure 2(*b*) illustrates the DNS (solid lines) and expansion (dash-dotted lines) results for t_{on} as a function of k. For a given ϵ, there is a maximum wavenumber above which onset of convection never occurs because the boundary layer stability increases at large wavenumbers. Agreement between the DNS and expansion is excellent and the solid and dash-dotted lines are virtually indistinguishable. Expansion (3.1), however, requires two orders of magnitude less computational time than DNS. On identical CPUs, the expansion results were computed in 4 h, while the DNS required 500 h.

The solid dots in figure 2(*b*) mark the minimum onset times, t_{on}^{min}, and corresponding wavenumbers, k_{on}^{min}, computed using expansion (3.1). The results are also presented in table 1. With increasing initial amplitude, onset of convection occurs sooner and k_{on}^{min} increases. We obtain the following quadratic fits for $(k_{on}^{min}, t_{on}^{min})$ as functions of $\log_{10}\epsilon$,

$$k_{on}^{min} \approx 0.1816(\log_{10}\epsilon)^2 + 3.312\log_{10}\epsilon + 36.49. \tag{4.1}$$

$$t_{on}^{min} \approx 0.04498(\log_{10}\epsilon)^2 - 0.8557\log_{10}\epsilon - 0.3850. \tag{4.2}$$

Note that relations (4.1) and (4.2) were obtained using the data in table 1 as well as data for $(k_{on}^{min}, t_{on}^{min})$ at four additional values of ϵ in the range $10^{-7} \leqslant \epsilon \leqslant 10^{-3}$. The fits produce errors on the order of 0.1 % with respect to table 1.

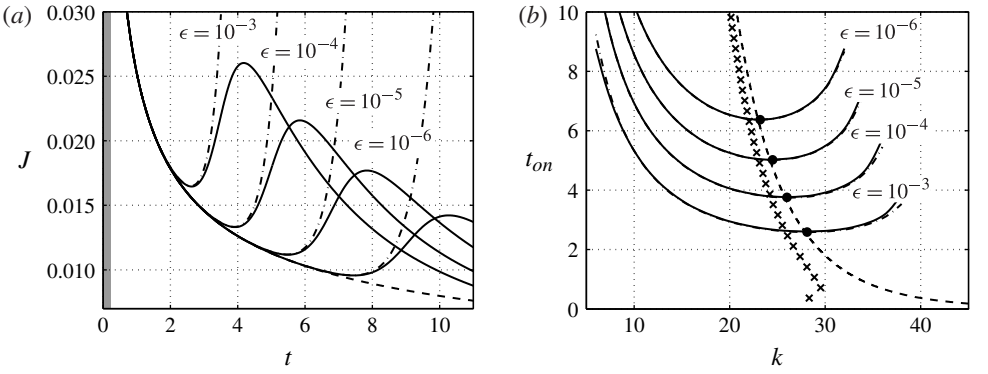

FIGURE 2. DNS and expansion (3.1) results for J and t_{on} when $Ra = 500$, $t_p = 0.01$ and $\epsilon = 10^{-3}$, 10^{-4}, 10^{-5} and 10^{-6}. (*a*) DNS (solid lines) and expansion (dash-dotted lines) results for J versus t when $k = 30$. The dashed line shows the flux J_b due to the base state. The initial damped period, $t < 0.219$, when $\mathrm{d}E_k/\mathrm{d}t < 0$, is shaded grey. (*b*) DNS (solid lines) and expansion (dashed-dotted lines) results for t_{on} versus k. Solid dots indicate $(k_{on}^{min}, t_{on}^{min})$. The dashed line shows the wavenumbers that maximize E_k. Note that these wavenumbers are indistinguishable from those that maximize E_k^c. The crosses show wavenumbers that maximize E_k^w.

ϵ	k_{on}^{min}	t_{on}^{min}	Φ_{cr}
1×10^{-3}	28.26	2.589	17.73
1×10^{-4}	26.09	3.756	1.542×10^{2}
1×10^{-5}	24.50	5.019	1.395×10^{3}
1×10^{-6}	23.20	6.371	1.292×10^{4}
1×10^{-7}	22.15	7.808	1.213×10^{5}

TABLE 1. For $Ra = 500$ and $t_p = 0.01$, the second, third and fourth columns present expansion results for k_{on}^{min}, t_{on}^{min} and Φ_{cr}, respectively, for the initial amplitudes, ϵ, presented in the first column.

The solid dots marking $(k_{on}^{min}, t_{on}^{min})$ in figure 2(*b*) lie virtually on the dashed line that shows the wavenumbers that maximize the amplitude of the fundamental mode, $E_k(t)$. This suggests, as expected, that onset of convection occurs due to perturbations that maximize E_k. Most previous studies of diffusive boundary layers measure perturbation amplitude with respect to either the vertical velocity field (Foster 1965; Gresho & Sani 1971; Kaviany 1984; Hassanzadeh, Pooladi-Darvish & Keith 2006) or concentration field (Caltagirone 1980; Ennis-King & Paterson 2003; Kim & Kim 2005; Riaz *et al.* 2006; Rapaka *et al.* 2008), as

$$E_k^w = \left[\frac{1}{\lambda_k}\int_0^{\lambda_k}\int_0^1 \frac{1}{2}\widetilde{w}_k^2 \,\mathrm{d}z\,\mathrm{d}x\right]^{1/2}, \quad E_k^c = \left[\frac{1}{\lambda_k}\int_0^{\lambda_k}\int_0^1 \frac{1}{2}\widetilde{c}_k^2 \,\mathrm{d}z\,\mathrm{d}x\right]^{1/2}. \tag{4.3}$$

There is significant disagreement in the literature concerning which of the two measures in (4.3) best predicts the dominant perturbations responsible for onset of convection. Repeating our analysis for E_k^c and E_k^w, we find that the wavenumbers that maximize E_k^c are indistinguishable from those that maximize E_k, and are consequently

good predictors of dominant perturbations. In future studies, it would be sufficient to measure perturbation magnitude with respect to only the concentration field. Because this result is not obvious from the previous literature, the current study uses definitions of ϵ and E_l that include both the velocity and concentration fields. In contrast to E_k^c, we find that E_k^w is not a good predictor of dominant perturbations. This is demonstrated in figure 2(*b*) where the crosses denote wavenumbers that maximize E_k^w. These do not accurately predict k_{on}^{min}.

For completeness, we repeat the computation of t_{on}^{min} and k_{on}^{min} by measuring the initial perturbation magnitude as $\epsilon^c = E_k^c(t_p)$. We find the following analogues to relations (4.1) and (4.2)

$$k_{on}^{min} \approx 0.1808(\log_{10}\epsilon^c)^2 + 3.316\log_{10}\epsilon^c + 36.57, \tag{4.4}$$

$$t_{on}^{min} \approx 0.04495(\log_{10}\epsilon^c)^2 - 0.8566\log_{10}\epsilon^c - 0.3983. \tag{4.5}$$

4.2. *The critical perturbation amplification for onset of nonlinear convection*

Previous linear stability analyses have suggested that perturbations must attain a critical magnitude to trigger the onset of nonlinear convection (Kaviany 1984; Kim & Kim 2005). Within the limitations of a linear analysis, this is suggested by expressing perturbation growth in terms of an amplification defined as $\Phi(k, t) = E_k(t)/E_k(t_p) = E_k(t)/\epsilon$. A critical amplification, Φ_{cr}, for onset of nonlinear convection can then be estimated by comparing linear results for $\Phi(k, t)$ with experimental results for t_{on}. The critical amplification is set to the linear result for the maximum amplification at $t = t_{on}$ (Kaviany 1984; Kim & Kim 2005). Previous linear and experimental studies, however, provide no information regarding the initial perturbation magnitude. Consequently, this approach provides a single value of Φ_{cr} for specific experimental conditions, and it neglects the intuitive result that Φ_{cr} should decrease as ϵ increases.

To investigate the notion of a critical perturbation amplification and magnitude, we first define the critical amplification as

$$\Phi_{cr} = \frac{E_{k_{on}^{min}}(t_{on}^{min})}{\epsilon}. \tag{4.6}$$

Here Φ_{cr} is simply the amplification measured at $(k_{on}^{min}, t_{on}^{min})$, see the solid dots in figure 2(*b*). Table 1 and figure 3(*a*) show Φ_{cr} as a function of ϵ. These demonstrate that for $Ra = 500$ and $t_p = 0.01$, Φ_{cr} satisfies the power law

$$\Phi_{cr} = 0.02280\epsilon^{-0.9591}. \tag{4.7}$$

As expected, perturbations with large initial magnitudes require less amplification to trigger nonlinear convection than initially small perturbations. This indicates that experimentally measured values of Φ_{cr} are only valid among systems with similar initial perturbation magnitudes. For example, if in physical systems, ϵ is determined by an aquifer's pore structure, then we expect that experimental values of Φ_{cr} should be valid for aquifers with similar pore composition. If, however, ϵ is sensitive to uncharacterizable flow conditions, then Φ_{cr} may vary widely among aquifers of similar structure.

We find that for a fixed initial perturbation magnitude, ϵ, onset of nonlinear convection occurs when perturbations attain a critical amplification that is independent of the perturbation wavenumber. This result is demonstrated by the dashed lines in figure 3(*b*) that show linear results for isocontours of the amplification $\Phi(k, t) = \Phi_{cr}$

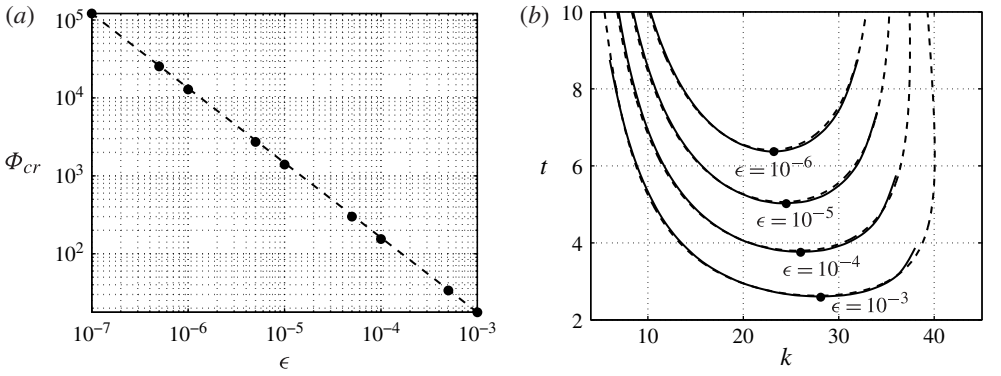

FIGURE 3. Results for the critical amplification Φ_{cr} when $t_p = 0.01$ and $Ra = 500$. (*a*) Expansion results for Φ_{cr} as a function of ϵ. The dashed line shows relation (4.7). (*b*) Isocontours of $\Phi = \Phi_{cr}$ (dashed lines) in the (k, t) plane for $\epsilon = 10^{-3}, 10^{-4}, 10^{-5}$ and 10^{-6}. The solid lines show the corresponding DNS results for t_{on} versus k. The solid dots show $(k_{on}^{min}, t_{on}^{min})$.

in the (k, t) plane when $\epsilon = 10^{-3}, 10^{-4}, 10^{-5}$ and 10^{-6}. Note that, by definition, these contours pass through the points $(k_{on}^{min}, t_{on}^{min})$, shown in figure 3(*b*) as solid dots. The solid lines in figure 3(*b*) show the corresponding DNS results for t_{on} as a function of k. We observe that the Φ isocontours are virtually indistinguishable from the DNS results for t_{on}. This means that for a fixed ϵ, onset of nonlinear convection occurs at the same value of amplification, $\Phi = \Phi_{cr}$, for all wavenumbers. The critical amplification can also be expressed as a critical magnitude $E_{cr} = \epsilon\Phi_{cr} = 0.0228\epsilon^{0.0409}$. The onset time, t_{on}, varies with k because the perturbation growth rate and the time required to attain E_{cr} vary with the wavenumber. The minimum onset time, t_{on}^{min}, occurs at the wavenumber, k_{on}^{min}, that first attains the critical magnitude, E_{cr}.

Note from figure 3(*b*) that at large wavenumbers, for example $k = 38$, the DNS results do not predict onset of nonlinear convection when the perturbation attains the critical magnitude E_{cr}. In these cases, nonlinear mechanisms cause only a small deviation of the flux, J, from that due to the base state, J_b, and do not produce a turning point $\mathrm{d}J/\mathrm{d}t = 0$ within the final time of the DNS, $t = 20$. In this case, an alternate definition of the onset time could be introduced to extend the DNS results to higher wavenumbers, such as the time t_{on}^{*} when the ratio $J/J_b = 1.01$. We, however, prefer to measure t_{on} with respect to the turning point where $\mathrm{d}J/\mathrm{d}t = 0$ because this is more clearly defined. Moreover, in physical systems, we do not expect to observe onset of convection at the large wavenumbers mentioned above, because onset will occur earlier at $(k_{on}^{min}, t_{on}^{min})$.

For completeness, we repeat our computation of the critical amplification by measuring the initial amplitude as $\epsilon^c = E_k^c(t_p)$, we report the following result,

$$\Phi_{cr}^c = 0.01751(\epsilon^c)^{-0.9573} \quad \text{where } \Phi_{cr}^c = \frac{E_{k_{on}^{min}}^c(t_{on}^{min})}{\epsilon^c}. \tag{4.8}$$

4.3. *Optimal initial perturbation time and minimum onset time*

In a previous linear stability analysis, Daniel *et al.* (2013) have shown that there is an optimal wavenumber and initial perturbation time that maximize the perturbation

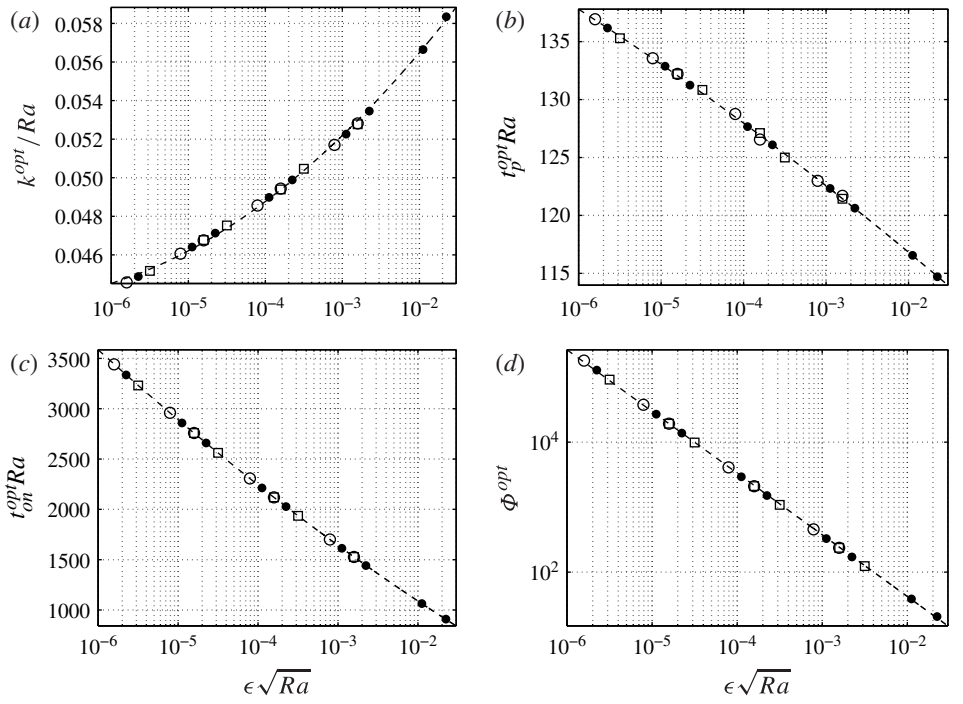

FIGURE 4. Expansion (3.1) results for (*a*) k^{opt}/Ra, (*b*) $t_p^{opt}Ra$, (*c*) $t_{on}^{opt}Ra$ and (*d*) Φ^{opt} as functions of $\epsilon\sqrt{Ra}$ for $Ra = 250$ (circles), 500 (solid dots) and 1000 (squares). The dashed lines show the corresponding best fits (4.9)–(4.12).

amplification, Φ, within the linear regime. Similarly, we find that for a given Rayleigh number, Ra, and initial perturbation magnitude, ϵ, there is an optimal wavenumber, k^{opt}, and initial time, t_p^{opt}, that minimize the onset time of nonlinear convection, t_{on}^{opt}. Furthermore, t_{on}^{opt} occurs when the perturbation amplification attains a critical value, Φ^{opt}. We compute k^{opt}, t_p^{opt}, t_{on}^{opt}, and Φ^{opt} for the Rayleigh numbers $Ra = 250$, 500 and 1000, and the initial perturbation magnitudes $\epsilon \geqslant 10^{-7}$, using expansion (3.1). Figure 4 demonstrates that the results collapse to four curves by plotting k^{opt}/Ra (figure 4*a*), $t_p^{opt}Ra$ (figure 4*b*), $t_{on}^{opt}Ra$ (figure 4*c*) and Φ^{opt} (figure 4*d*) as functions of $\epsilon\sqrt{Ra}$. The dashed lines show the following best fits,

$$\frac{k^{opt}}{Ra} = 4.328 \times 10^{-4} \left[\log_{10}\left(\epsilon\sqrt{Ra}\right)\right]^2 + 6.453 \times 10^{-3} \log_{10}\left(\epsilon\sqrt{Ra}\right) + 0.06765, \quad (4.9)$$

$$t_p^{opt}Ra = -0.1623 \left[\log_{10}\left(\epsilon\sqrt{Ra}\right)\right]^2 - 6.544 \log_{10}\left(\epsilon\sqrt{Ra}\right) + 104.4, \quad (4.10)$$

$$t_{on}^{opt}Ra = 23.84 \left[\log_{10}\left(\epsilon\sqrt{Ra}\right)\right]^2 - 433.3 \log_{10}\left(\epsilon\sqrt{Ra}\right) + 127.4, \quad (4.11)$$

$$\Phi^{opt} = 0.5370 \left(\epsilon\sqrt{Ra}\right)^{-0.9486}. \quad (4.12)$$

The results in figure 4 collapse because for $Ra \geqslant 250$ and $\epsilon \geqslant 10^{-7}$, onset of nonlinear convection occurs before the flow fields interact with the lower boundary. Consequently, the Rayleigh number dependence may be removed by approximating the aquifer depth as infinite, $H \to \infty$, and non-dimensionalizing the governing equations

(2.1)–(2.4) with respect to the characteristic length $L^* = \phi\mathscr{D}/U$ and time $T^* = \phi L^*/U$. Recall from § 2 that $U = K\Delta\rho g/\mu$. One can then show that a system characterized by the parameters $(Ra_1,\ t_{p1},\ \epsilon_1)$ is equivalent to a second system characterized by $(Ra_2,\ t_{p2},\ \epsilon_2)$ provided that $t_{p1}Ra_1 = t_{p2}Ra_2$ and $\epsilon_1\sqrt{Ra_1} = \epsilon_2\sqrt{Ra_2}$. We conclude that prior to interaction with the lower wall, onset of nonlinear convection in a system with a large Rayleigh number is equivalent to onset of convection in a system with a smaller Rayleigh number, later initial perturbation time, and larger initial perturbation amplitude. Note that relation (4.12) for Φ^{opt} differs from relation (4.7) for Φ_{cr} because the latter is computed for $t_p = 0.01$, while the former is computed for $t_p = t_p^{opt}$.

The notion of an optimal initial perturbation time may appear counterintuitive because in physical systems, boundary layers are often continuously perturbed from $t_p = 0$ onwards. An optimal perturbation time occurs because perturbations originating near $t_p = 0$ are damped up to the critical time for linear instability, t_c. Consequently, they have smaller late-time magnitudes than perturbations originating near $t_p \approx t_c$. Conversely, perturbations originating at late times, $t \gg t_c$ may grow immediately, but have smaller magnitudes than perturbations that began growing at earlier times near $t_p \approx t_c$. If within the linear regime, $t < t_{on}$, the response to continuous forcing can be expressed as the infinite sum of many impulse responses to forcing at discrete initial times, then t_{on}^{opt} represents a theoretical minimum onset time produced by the initial perturbation profile $c_p(z)$ given in (2.6).

To facilitate their application to physical systems, relations (4.9)–(4.11) can be rewritten in dimensional form as

$$\frac{k^*\phi\mathscr{D}}{U} = 4.804\times10^{-4}(\log_{10}\epsilon^*)^2 + 6.968\times10^{-3}\log_{10}\epsilon^* + 0.06936, \tag{4.13}$$

$$\frac{t_p^*U^2}{\phi^2\mathscr{D}} = -0.2241(\log_{10}\epsilon^*)^2 - 7.363\log_{10}\epsilon^* + 113.0, \tag{4.14}$$

$$\frac{t_{on}^*U^2}{\phi^2\mathscr{D}} = 23.76(\log_{10}\epsilon^*)^2 - 432.1\log_{10}\epsilon^* + 89.75, \tag{4.15}$$

where k^*, t_p^* and t_{on}^* are the dimensional optimal wavenumber, initial time and onset time, respectively. Relations (4.13)–(4.15) have been expressed in terms of an initial perturbation magnitude measured with respect to the concentration field as

$$\epsilon^* = E_k^c(t_p)\sqrt{Ra} = \left\{\frac{U}{\phi\mathscr{D}}\int_0^H\left(\frac{c_p^*}{C_1}\right)^2\mathrm{d}z\right\}^{1/2}, \tag{4.16}$$

where E_k^c is defined in (4.3), $c_p^*(z)$ is the dimensional initial perturbation profile, and C_1 is the concentration at $z = 0$. The initial magnitude (4.16) facilitates the application of (4.13)–(4.15) because it requires only the initial concentration field. Though H appears in the integral of (4.16), relations (4.13)–(4.16) are actually independent of H because $c_p^*(z)$ is concentrated near $z = 0$, see figure 1(*b*).

Ennis-King & Paterson (2003) cite the following typical parameter values for CO_2 sequestration: $\mu = 5\times10^{-4}$ Pa s, $\phi = 0.2$, $\Delta\rho = 10$ kg m^{-3}, $g = 9.81$ m s^{-2}, $\mathscr{D} = 10^{-9}$ m^2 s^{-1} and $10^{-14} \leqslant K \leqslant 10^{-12}$ m^2. Using these values for a high-permeability aquifer, $K = 10^{-12}$ m^2, relations (4.13)–(4.16) predict that the optimal wavelength, initial time, and onset time vary between $2\pi/k^* = 12.14$ cm, $t_p^* = 38.41$ h, $t_{on}^* = 461.8$ h for $\epsilon^* = 10^{-3}$ and $2\pi/k^* = 14.28$ cm, $t_p^* = 43.04$ h, $t_{on}^* = 1021$ h for $\epsilon^* = 10^{-6}$. For a low-permeability aquifer, $K = 10^{-14}$ m^2, the parameters vary

between $2\pi/k^* = 12.14$ m, $t_p^* = 43.85$ years, $t_{on}^* = 527.1$ years for $\epsilon^* = 10^{-3}$ and $2\pi/k^* = 14.28$ m, $t_p^* = 49.13$ years, $t_{on}^* = 1165$ years for $\epsilon^* = 10^{-6}$. As expected, t_{on}^* increases with decreasing permeability and initial perturbation magnitude. We observe, however, that t_{on}^* is far more sensitive to changes in permeability than ϵ^*. We note similar trends for t_p^*. The optimal wavenumber increases with permeability but decreases with ϵ^*. These trends for t_p^* and k^* agree well with those observed by Daniel *et al.* (2013). In that study, Daniel *et al.* (2013) showed that for given aquifer parameters, there is an optimal wavenumber, k, initial time, t_p, and perturbation profile, $c_p(z)$, that maximize the perturbation amplification, Φ, predicted by linear theory at a given final time, $t = t_f$. Due to the limitations of linear theory, Daniel *et al.* (2013) could not explore the dependence of the optimal perturbation profile, c_p, on the initial perturbation magnitude. Although beyond the scope of the current study, this could be achieved using expansion (3.1).

5. Perturbation evolution after onset of nonlinear convection

This section explores perturbation evolution after the onset of nonlinear convection. In § 5.1, we consider systems perturbed with a single Fourier mode. We explain the deviation of expansion (3.1) from DNS results and comment on whether more sophisticated expansions could better approximate perturbation evolution beyond $t = t_{on}$. In § 5.2, we consider systems in which many Fourier modes are simultaneously perturbed. We demonstrate that following the onset of nonlinear convection, $t > t_{on}$, these systems are qualitatively very different from systems perturbed with single modes.

Results in this section are computed using the Rayleigh number $Ra = 500$. Although we consider times $t \leqslant 15$, the end-effects due to the impermeable wall at $z = 1$ are likely important for times $t > 10$. Consequently, the physical relevance of results for times $t > 10$ should be evaluated in the context of the approximate boundary conditions (2.2) for flow at an interface between a porous medium and an impermeable boundary.

5.1. *Systems perturbed with a single Fourier mode*

To investigate the evolution of perturbations after the onset of nonlinear convection, we consider a boundary layer of Rayleigh number $Ra = 500$ that is perturbed with the Fourier mode $k = 30$ at the initial time $t_p = 0.01$ with initial magnitude $\epsilon = 10^{-5}$. Figure 5(*a*) compares DNS and expansion results for the evolution of the fundamental mode, $E_{30}(t)$, and the zero-wavenumber response $E_0(t)$. DNS results are shown using a solid line for E_{30} and a dashed line for E_0. Expansion results are shown using circles for E_{30} and squares for E_0. The linear regime $t < t_{on}$ (where $t_{on} = 5.487$) is shaded grey. For brevity, results for the second harmonic, E_{60}, are not shown. Recall that the DNS results for E_{30} and E_0 are computed using the norm (3.18), while the expansion results are computed using (3.19). The perturbation magnitudes predicted by expansion (3.1) agree with DNS within the shaded linear regime of figure 5(*a*). After t_{on}, however, expansion (3.1) overpredicts the magnitudes and experiences breakdown near $t \approx 7$. We use the term 'breakdown' as defined by Nayfeh (1981) to denote when a higher-order correction term becomes equal order with a lower-order term, thereby violating the assumptions of the expansion. In figure 5(*a*), the expansion breaks down when the expansion results for E_0 (squares) and E_{30} (circles) become equal order. Note that the breakdown of expansion (3.1) is not related to the transient nature of the base state $c_b(z, t)$. In fact, a regular asymptotic expansion of RB convection would

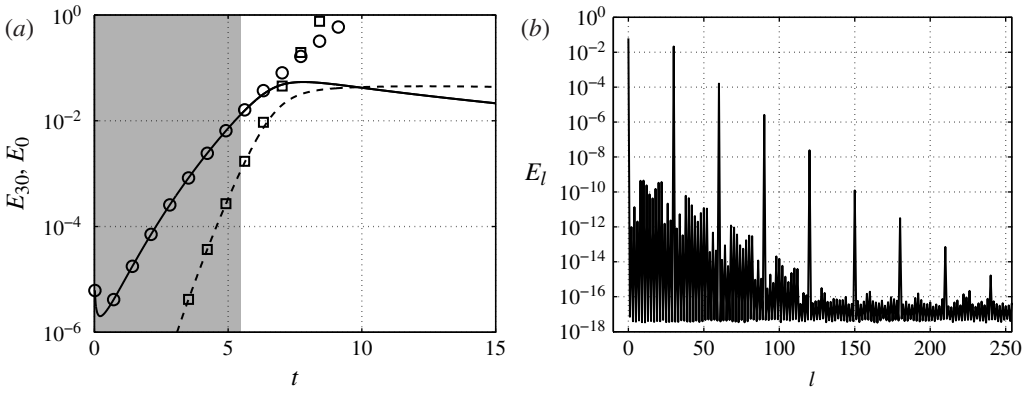

FIGURE 5. DNS and expansion results for the perturbation amplitudes when $Ra = 500$, $t_p = 0.01$, $k = 30$ and $\epsilon = 10^{-5}$. (*a*) The solid line and dashed line show DNS results for E_{30} and E_0, respectively. The circles and squares show expansion results for E_{30} and E_0 respectively. The linear regime $t < t_{on}$, where $t_{on} = 5.487$, is shaded grey. (*b*) Plot of E_l versus wavenumber l, at $t = 15$.

similarly break down. The breakdown occurs because the first-order problem (3.5) and (3.6) generated by expansion (3.1) evolves independently of the higher-order problems and consequently cannot account for the nonlinear saturation of the fundamental mode. A further interpretation is that expansion (3.1) only captures the linear regime up to $t = t_{on}$. For this reason, we also refrain from referring to expansion (3.1) as a 'weakly nonlinear expansion'. Taking expansion (3.1) to order $\mathcal{O}(\epsilon^3)$ does not improve the expansion's prediction of t_{on}.

Turning our attention to the DNS results illustrated in figure 5(*a*), we observe that after the onset of nonlinear convection, $t > t_{on}$, the DNS results for the magnitude of the fundamental mode, E_{30} (solid line), attain a maximum when $t \approx 7.8$, after which E_{30} decreases. Meanwhile, the DNS results for E_0 (dashed-line) become equal order with the DNS results for E_{30} (solid line) around $t \approx 7$. Subsequently, E_0 plateaus to a nearly constant value that is greater than E_{30}. This growth of the zero-wavenumber mode, such that it surpasses the fundamental, is not observed in corresponding DNS of weakly supercritical RB convection. In that case, the magnitude of the fundamental, E_k, and the zero-wavenumber mode, E_0, saturate to constant values for which $E_0 \ll E_k$. This is demonstrated in appendix B where we perform DNS of weakly supercritical RB convection in a porous layer. In the case of weakly supercritical RB convection, the fact that E_0 remains small compared with E_k allows the late-time perturbation evolution to be readily modelled using a Lindstedt–Poincaré technique or multiple-scale expansion (Malkus & Veronis 1958; Palm 1960; Godreche & Manneville 1998). For the current problem, however, the application of these methods may not be straightforward because our DNS results indicate that the usual assumption that $E_0 \ll E_k$ must be relaxed. We do not pursue these methods, however, because the results of § 5.2 suggest that they are not relevant to physical systems in which many Fourier modes are simultaneously perturbed. It should also be stressed that the DNS results for E_0 (dashed line) and E_{30} (solid line) in figure 5(*a*) are entirely physical, and should not be confused with the unphysical breakdown of expansion (3.1).

We offer the following interpretation of the DNS results presented in figure 5(*a*). In the case of RB convection, the Rayleigh number is a parameter that can be fixed

experimentally such that the flow remains weakly supercritical, $0 \leqslant Ra - Ra_c \ll 1$. As a consequence, unstable perturbations have only small growth rates, where the growth rate is defined as $\sigma = E_k^{-1}(\mathrm{d}E_k/\mathrm{d}t)$. In appendix B, we find the maximum growth rates produced by weakly supercritical RB convection are of the order $\sigma \sim \mathscr{O}(0.1)$ or less. For the current problem, however, the growth rates of unstable perturbations are small only near the critical time, i.e. $0 \leqslant t - t_c \ll 1$. In figure 5(*a*), the critical time occurs at $t_c = 0.219$, where $\mathrm{d}E_{30}/\mathrm{d}t = 0$. Because the critical parameter for instability is a time, $t = t_c$, there is no way for the flow to remain weakly supercritical. In contrast, following the onset of linear instability, $t > t_c$, the instability of the boundary layer increases rapidly such that the perturbation growth rate exceeds $\sigma = 2$ when $t = 1$ (for details, see figure 7(*a*) of Tilton *et al.* 2013).

To provide further physical interpretation of the DNS results in figure 5(*a*), we consider figure 5(*b*) that shows DNS results for E_l as a function of the wavenumber, l, at the late time $t = 15$. Recall from (3.18) that E_l represents the magnitude of each horizontal Fourier mode l of the perturbation flow field. Figure 5(*b*) demonstrates that the late-time perturbation magnitude is concentrated in the fundamental and zero wavenumbers. The magnitude of the higher harmonics, however, are much smaller and exhibit a clear separation of orders with increasing harmonic index, i.e. $E_{60} \gg E_{90} \gg E_{120}$. Consequently, the problem can be modelled using the reduced nonlinear IVP method previously used by Jhaveri & Homsy (1982) in a study of thermal convection in fluid layers,

$$\begin{bmatrix} c \\ u \\ w \end{bmatrix} \approx \begin{bmatrix} c_b(z,t) + \widehat{c}_m(z,t) \\ 0 \\ 0 \end{bmatrix} + \begin{bmatrix} \widehat{c}_k(z,t)\left(\mathrm{e}^{\mathrm{i}kx} + \mathrm{e}^{-\mathrm{i}kx}\right) \\ \mathrm{i}\widehat{u}_k(z,t)\left(\mathrm{e}^{\mathrm{i}kx} - \mathrm{e}^{-\mathrm{i}kx}\right) \\ \widehat{w}_k(z,t)\left(\mathrm{e}^{\mathrm{i}kx} + \mathrm{e}^{-\mathrm{i}kx}\right) \end{bmatrix}, \tag{5.1}$$

where $\widehat{u}_k = (1/k)(\partial \widehat{w}_k/\partial z)$. Approximation (5.1) is similar to expansion (3.1), but makes no assumptions about the relative magnitudes of the fundamental mode, $\widehat{c}_k$, and zero-wavenumber mode, $\widehat{c}_m$. The subscript m refers to the fact that previous literature often describes the zero-wavenumber mode as a modification of the mean concentration. Substituting (5.1) into (2.1)–(2.4), we find that

$$\frac{\partial \widehat{c}_k}{\partial t} + \widehat{w}_k\left(\frac{\partial c_b}{\partial z} + \frac{\partial \widehat{c}_m}{\partial z}\right) - \frac{1}{Ra}\left(\frac{\partial^2}{\partial z^2} - k^2\right)\widehat{c}_k = 0, \quad \left(\frac{\partial^2}{\partial z^2} - k^2\right)\widehat{w}_k = -k^2\widehat{c}_k, \tag{5.2}$$

$$\frac{\partial \widehat{c}_m}{\partial t} - \frac{1}{Ra}\frac{\partial^2 \widehat{c}_m}{\partial z^2} + 2\frac{\partial}{\partial z}(\widehat{w}_k\widehat{c}_k) = 0, \tag{5.3}$$

$$\widehat{c}_k\Big|_{z=0} = \widehat{c}_m\Big|_{z=0} = \widehat{w}_k\Big|_{z=0} = \frac{\partial \widehat{c}_k}{\partial z}\Big|_{z=1} = \frac{\partial \widehat{c}_m}{\partial z}\Big|_{z=1} = \widehat{w}_k\Big|_{z=1} = 0, \tag{5.4}$$

$$\widehat{c}_k\Big|_{t=t_p} = \epsilon c_p(z), \quad \widehat{c}_m\Big|_{t=t_p} = 0. \tag{5.5}$$

Figure 6 compares DNS and nonlinear IVP results when $Ra = 500$, $k = 30$, $t_p = 0.01$ and $\epsilon = 10^{-5}$. There is excellent agreement for the late-time evolution of J, E_{30} and E_0. We conclude that nonlinear interactions between the fundamental and zero-wavenumber modes are the dominant mechanisms responsible for perturbation evolution after $t = t_{on}$. The deviation of E_{30} (solid line) in figure 6(*b*) from that predicted by linear theory is due to the term $\widehat{w}_k(\partial \widehat{c}_m/\partial z)$ in (5.2) that modifies the fundamental harmonic and attenuates the growth of E_k. This then reduces the term $\partial(\widehat{w}_k\widehat{c}_k)/\partial z$ in (5.3), thereby attenuating the growth of E_0. Note that (5.2) and (5.3)

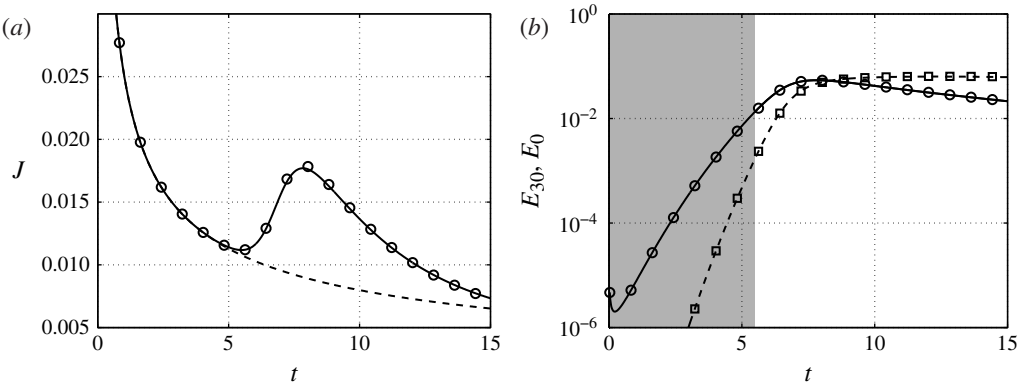

FIGURE 6. Comparison of DNS results with the reduced nonlinear IVP (5.2) and (5.3) when $Ra = 500$, $t_p = 0.01$, $k = 30$ and $\epsilon = 10^{-5}$. (*a*) DNS (solid line) and nonlinear IVP (circles) results for J versus t. The dashed line shows J_b. (*b*) DNS (solid line) and nonlinear IVP (circles) results for E_{30}. DNS (dashed line) and nonlinear IVP (squares) results for E_0. The linear regime $t < t_{on}$, where $t_{on} = 5.487$, is shaded grey.

depend on ϵ through initial condition (5.5). Consequently, we find the nonlinear IVP method requires one order of magnitude more time than expansion (3.1) for the computation of t_{on}^{min} and k_{on}^{min}.

5.2. *Simultaneous perturbation of many wavenumbers*

To date, the linear stability of transient diffusive boundary layers has been studied almost exclusively by perturbing individual horizontal Fourier modes. This assumes the least stable mode will dominate the linear regime and trigger the onset of nonlinear convection. In physical systems, however, many horizontal modes can be simultaneously perturbed. As these simultaneous modes grow temporally, their nonlinear interactions may eventually bypass the linear path to onset of nonlinear convection. The late-time perturbation evolution beyond $t = t_{on}$ may also be quite different from that predicted by DNS of cases for which a single Fourier mode is perturbed at $t = t_p$. Consequently, the physical relevance of individually perturbed Fourier modes must be considered.

To investigate these issues, we perform DNS of systems in which many horizontal Fourier modes are simultaneously perturbed at $t = t_p$ using the initial condition

$$c\big|_{t=t_p} = c_b(z, t_p) + c_p(z) \sum_{k=1}^{N_x/2-1} a_k \cos(kx + \phi_k), \tag{5.6}$$

where N_x is the number of horizontal collocation points, ϕ_k are randomly generated phases varying between $0 \leqslant \phi_k \leqslant L$, and a_k are coefficients computed so each horizontal mode is perturbed with equal initial magnitude, ϵ. The total initial perturbation magnitude, ϵ_T, is related to the initial magnitude of each mode, ϵ, through Parseval's theorem, $\epsilon_T = \epsilon\sqrt{N_x/2 - 1}$. All DNS in this section are performed for $t_p = 0.01$, $Ra = 500$, $L = 2\pi$ and $N_x = 512$. Consequently, all DNS resolve the integer wavenumbers $0 \leqslant k \leqslant 255$.

Figure 7(*a*) illustrates DNS results for the temporal evolution of the perturbation magnitudes, E_k, of the first 51 modes, $0 \leqslant k \leqslant 50$, for $\epsilon_T = 10^{-4}$ ($\epsilon = 6.26 \times 10^{-6}$).

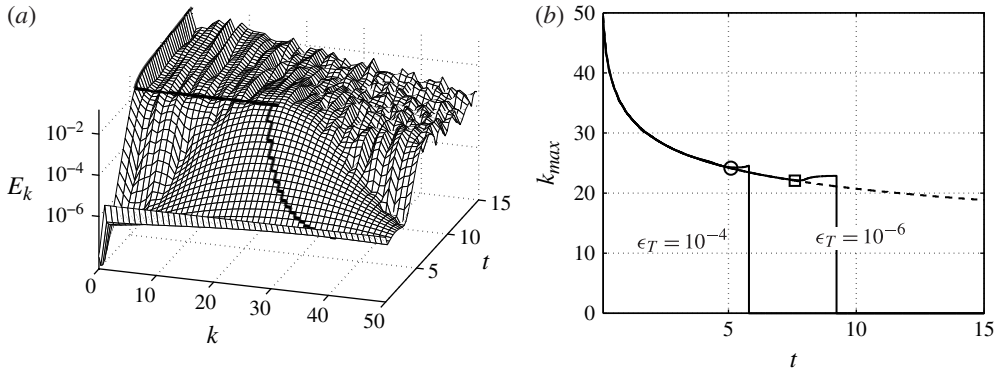

FIGURE 7. DNS results for the perturbation magnitude and dominant wavenumber using initial condition (5.6) with $t_p = 0.01$ and $Ra = 500$. (*a*) The perturbation magnitude E_k of modes $0 \leqslant k \leqslant 50$ as a function of t for $\epsilon_T = 10^{-4}$. The solid black line shows the dominant wavenumbers, k_{max}, that maximize E_k. (*b*) The temporal evolution of k_{max} for initial amplitudes $\epsilon_T = 10^{-4}$ and 10^{-6}. The dashed line shows the dominant wavenumbers predicted by linear theory. The circle and square mark the dominant wavenumbers $k_{on}^{min} = 24.17$ and $k_{on}^{min} = 22.06$, respectively, predicted by relation (4.1).

The thick black line shows the dominant wavenumbers, k_{max}, that maximize E_k. Initial amplitudes greater that $\epsilon_T = 10^{-4}$ are not considered because they produce negative initial concentrations. The magnitude of the zero-wavenumber mode is initially zero, $E_0 = 0$, because it is not perturbed by (5.6). The results in figure 7(*a*) may appear counterintuitive to readers accustomed to DNS of weakly supercritical RB convection. For this reason, we stress that tests were performed to confirm that aliasing, from the computation of nonlinear terms, did not affect our results.

In figure 7(*a*), we observe three regimes: (i) an initial regime during which perturbations are damped for all non-zero wavenumbers; (ii) a subsequent regime during which E_k increases such that the E_k surface in the $k - t$ plane is smooth; (iii) a final regime in which strongly nonlinear interactions produce an irregular E_k surface, and the perturbation amplitude is increasingly concentrated near the zero wavenumber, $k = 0$. During regimes (i) and (ii), the dominant wavenumbers decrease from initial values near $k = 50$ to values near $k = 25$. Sometime between regimes (ii) and (iii), k_{max} decreases discontinuously to $k_{max} = 0$ due to the growth of the zero-wavenumber mode.

We find that in regimes (i) and (ii), nonlinear interactions between individually perturbed modes are negligible, and the evolution of the E_k surface shows excellent agreement with that predicted by linear theory for individually perturbed Fourier modes. Figure 7(*b*) shows DNS results for the temporal evolution of k_{max} when the boundary layer is perturbed with condition (5.6) for $\epsilon_T = 10^{-4}$ and 10^{-6}. The variation of k_{max} has been smoothed by cubic interpolation of the DNS results. For comparison, the dashed line shows the dominant wavenumbers predicted by linear theory. The circle and square in figure 7(*c*) mark the dominant wavenumbers, k_{on}^{min}, for onset of convection, predicted by expansion (3.1) through relation (4.1). Relation (4.1) predicts $k_{on}^{min} = 24.17$ for $\epsilon_T = 10^{-4}$ ($\epsilon = 6.26 \times 10^{-6}$) and $k_{on}^{min} = 22.06$ for $\epsilon_T = 10^{-6}$ ($\epsilon = 6.26 \times 10^{-8}$). We observe that (4.1) accurately predicts the wavenumber at which DNS results for systems with simultaneously perturbed modes begin to deviate from linear theory due to onset of convection.

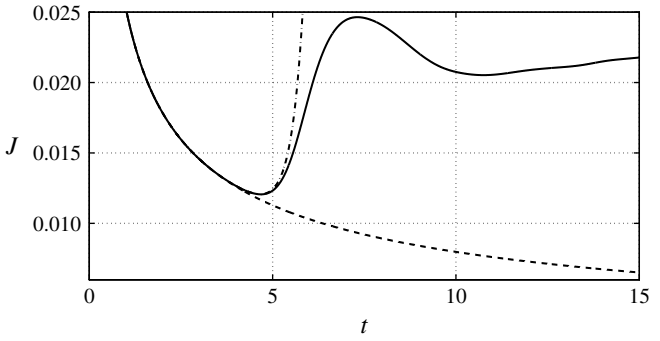

FIGURE 8. DNS result (solid line) for the flux, J, when the boundary layer is perturbed with condition (5.6) at $t_p = 0.01$, for $Ra = 500$ and $\epsilon_T = 10^{-4}$. The dashed line shows the flux J_b due to the base state. The dash-dotted line shows the expansion (3.1) result for J_s, see (5.7).

Figure 8 presents DNS results (solid line) for the flux when the system is perturbed with condition (5.6) for $\epsilon_T = 10^{-4}$. The dashed line shows the flux J_b due to the base state. The DNS result for the onset time, $t_{on} = 4.682$, is smaller than the minimum value, $t_{on}^{min} = 5.285$, predicted by expansion (3.1) through relation (4.2). The discrepancy occurs because when many Fourier modes are simultaneously perturbed, each mode contributes a zero-wavenumber response, $\widehat{c}_2^{(0)}$, predicted by expansion (3.1). To demonstrate this, we solve expansion (3.1) for the integer wavenumbers $10 \leqslant k \leqslant 40$ and sum their individual contributions to the total flux,

$$J_s = J_b + \sum_{k=10}^{40} \widetilde{J}_k, \tag{5.7}$$

where $\widetilde{J}_k$ is the increase in flux predicted by expansion (3.1) for mode k. Figure 8 demonstrates that J_s (dash-dotted line) correctly predicts the onset time, t_{on}, produced by simultaneously perturbed modes. As expected, the onset time in a physical system necessarily depends on which wavenumbers are naturally perturbed. Expansion (3.1) can be used to provide theoretical minimum onset times through relation (4.2) for t_{on}^{min} or relation (4.15) for t_{on}^{opt}.

Turning our attention to the nonlinear regime (iii) illustrated in figure 7(*a*), we note that the non-zero wavenumbers that dominate the linear regime do not appear to dominate the subsequent nonlinear regime. Rather, the perturbation magnitude in the nonlinear regime is concentrated in the zero-wavenumber mode, and there is no clearly dominant non-zero wavenumber. This suggests that, after the onset of nonlinear convection, the dynamics of transient diffusive boundary layers cannot be captured by considering an asymptotic expansion about a single fundamental mode. This is contrary to the case of RB convection. Similarly, although the nonlinear IVP of Jhaveri & Homsy (1982) captures the late-time evolution of individually perturbed modes, see figure 6, this late-time behaviour may not be relevant to physical systems with simultaneously perturbed modes. The absence of a clearly defined, dominant, non-zero wavenumber in the nonlinear regime (iii) of figure 7(*a*) may be related to the fact that prior to onset of convection, there is a band of unstable wavenumbers with large growth rates on the order of $\sigma \sim \mathscr{O}(1)$, where $\sigma = E_k^{-1}(\mathrm{d}E_k/\mathrm{d}t)$ (see Riaz *et al.* 2006; Tilton *et al.* 2013). In contrast, the weakly supercritical RB convection considered in appendix B has unstable growth rates on the order of $\sigma \sim \mathscr{O}(0.1)$.

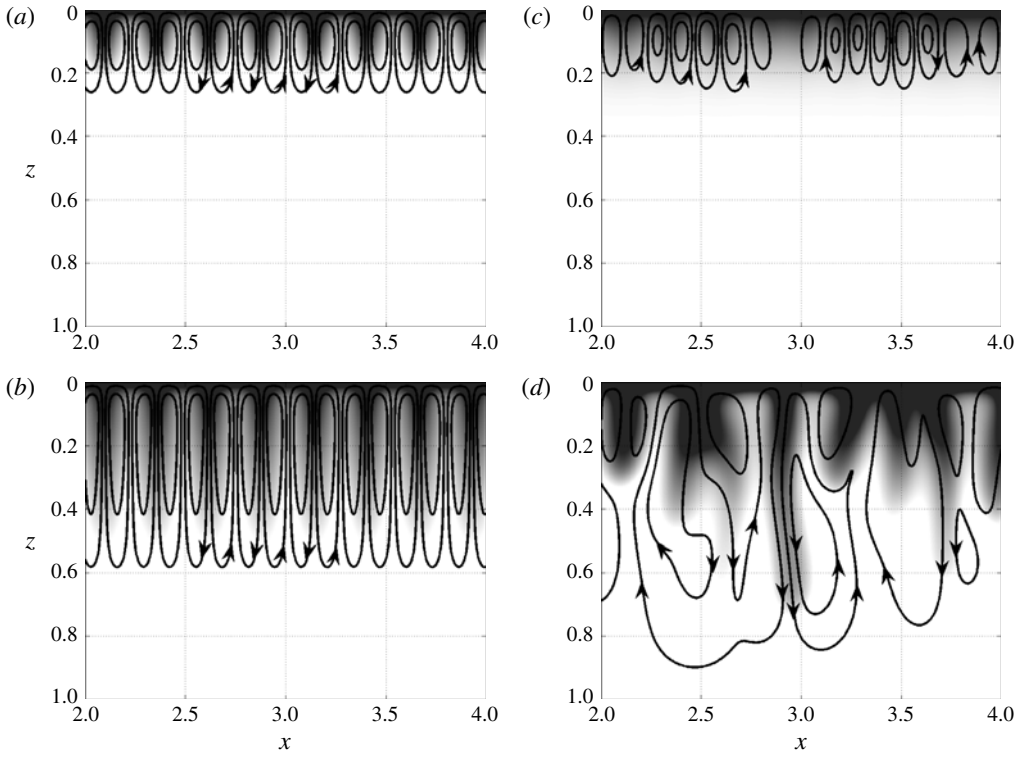

FIGURE 9. Comparison of the DNS results for the concentration contours (shaded grey) and streamlines (solid lines) when the boundary layer is perturbed with a single $k = 24$ Fourier mode with $\epsilon = 6.26 \times 10^{-4}$ (a, b) and when the boundary layer is perturbed with many Fourier modes using condition (5.6) with $\epsilon_{\mathrm{T}} = 10^{-4}$ $(\epsilon = 6.26 \times 10^{-4})$ (c, d). Both simulations set $t_p = 0.01$ and $Ra = 500$. Results are shown for times $t = 4.61$ (a, c) and $t = 10.01$ (b, d).

Figure 9(*a*,*b*) illustrates DNS results for the concentration contours (shaded grey) and streamlines (solid lines) when the transient diffusive boundary layer, c_b, is perturbed with the single Fourier mode $k = 24$ at $t_p = 0.01$ for $Ra = 500$ and $\epsilon = 6.26 \times 10^{-6}$. Results are shown for times $t = 4.61$ (figure 9*a*) and $t = 10.01$ (figure 9*b*). Figure 9(*c*,*d*) shows the corresponding results when the boundary layer is perturbed with many Fourier modes using condition (5.6) with $\epsilon_{\mathrm{T}} = 10^{-4}$. The time $t = 4.61$ is just prior to the onset time $t_{on} = 4.681$ for the system perturbed with initial condition (5.6). We observe that prior to onset of convection, DNS results for a single mode are representative of the perturbation structures observed when the system is perturbed with many modes. The results for $t = 10.01$, however, demonstrate that DNS results for single modes do not produce the late-time merging and splitting of fingers observed when systems are perturbed with many modes.

6. Summary and conclusions

We have investigated the onset of nonlinear convection in transient diffusive boundary layers in homogeneous isotropic porous media. We demonstrated that the onset time of nonlinear convection, t_{on}, can be accurately determined (within 1 % of

DNS) from a regular asymptotic expansion that is one order of magnitude faster than the method of Jhaveri & Homsy (1982) and two orders of magnitude faster than DNS. We then used the expansion to study t_{on} in terms of the initial perturbation magnitude, ϵ, initial perturbation time, t_p, wavenumber, k, and Rayleigh number, Ra. After onset of nonlinear convection, the expansion breaks down due to secular terms. Consequently, we explored late-time perturbation evolution, $t > t_{on}$, using high-order DNS and the method of Jhaveri & Homsy (1982). We also compared boundary layers perturbed with a single Fourier mode to those simultaneously perturbed with many modes.

To be consistent with previous stability analyses, we first considered boundary layers perturbed with a single Fourier mode at a fixed initial time that is much smaller than the critical time for linear instability, $t_p \ll t_c$. We showed that for these cases, onset of nonlinear convection occurs when a perturbation attains a critical amplification, Φ_{cr}, that is independent of the perturbation's wavenumber. Consequently, the minimum onset time, t_{on}^{min}, occurs at the wavenumber k_{on}^{min} for which perturbations first attain Φ_{cr}. We found analytical relationships for k_{on}^{min}, t_{on}^{min} and Φ_{cr} in terms of the initial perturbation magnitude, see (4.1), (4.2) and (4.7). These show that perturbations with large initial amplitudes have smaller onset times t_{on}^{min}, larger wavenumbers k_{on}^{min}, and smaller critical amplifications Φ_{cr} than perturbations with small initial magnitudes. Finally, we compared two competing measures of perturbation magnitude that respectively measure the perturbation concentration field, E_k^c, and vertical velocity field, E_k^w, see (4.3). These measures have produced considerable disagreement in the previous literature. We found that perturbations that maximize E_k^c accurately predict the wavenumbers k_{on}^{min}. This supports previous studies that measure perturbation growth with respect to the concentration field (Caltagirone 1980; Ennis-King & Paterson 2003; Kim & Kim 2005; Riaz *et al.* 2006; Rapaka *et al.* 2008). We found, however, that perturbations that maximize E_k^w do not accurately predict k_{on}^{min}. This brings into question the results of studies that measure perturbation growth with respect to the vertical velocity field (Foster 1965; Gresho & Sani 1971; Kaviany 1984; Hassanzadeh *et al.* 2006).

After considering a fixed initial perturbation time, we then varied t_p to show that there is an optimal combination of initial time, t_p^{opt}, and wavenumber, k^{opt}, that minimize the onset time of nonlinear convection, t_{on}^{opt}. Furthermore, onset occurs at a critical amplification, Φ^{opt}. By rescaling the problem, we obtained analytical relationships for these optimal parameters in terms of aquifer properties and the initial perturbation magnitude. To the best of the authors' knowledge, such relationships have been lacking to date and represent a major contribution to modelling CO_2 sequestration. Furthermore, these relationships show the importance of the initial perturbation time and magnitude, which are often overlooked in previous studies. We demonstrate that for typical aquifers, the dimensional optimal initial time, t_p^*, and corresponding dimensional onset time, t_{on}^*, can both decrease by several orders-of-magnitude with increasing permeability and initial perturbation magnitude. We observe, however, that t_p^* and t_{on}^* are far more sensitive to variations of the permeability than variations of the initial perturbation magnitude.

We found that when a boundary layer is perturbed with a single Fourier mode, the late-time perturbation evolution, $t > t_{on}$, is dominated by nonlinear interactions between the fundamental mode and the zero-wavenumber response. DNS showed that the magnitude of the zero-wavenumber mode, E_0, becomes equal-order with the fundamental mode, E_k. This indicates that the application of multiple-scale methods to transient diffusive boundary layers may not be straightforward because the assumption

that $E_0 \ll E_k$ must be relaxed. We showed, however, that the nonlinear IVP of Jhaveri & Homsy (1982) shows excellent agreement with DNS for the late times $t > t_{on}$. The agreement occurs because the method of Jhaveri & Homsy (1982) assumes the zero-wavenumber response is equal order with the fundamental mode.

We demonstrated through DNS that when a boundary layer is simultaneously perturbed with many Fourier modes, there is an initial linear regime, $t < t_{on}$, during which nonlinear interactions between simultaneously perturbed modes can be ignored. The analytical relationships produced by our expansion correctly predict the dominant wavenumber for onset of nonlinear convection, but underpredict t_{on}. The discrepancy occurs because each perturbed mode contributes to the increase in the flux J. The discrepancy can be removed by simply summing the flux contributions of each of the perturbed modes, see (5.7). After the onset of nonlinear convection, however, these systems are dominated by strongly nonlinear interactions between simultaneously perturbed modes. Furthermore, the perturbation magnitude is concentrated in the zero-wavenumber mode, and there is no clearly dominant, non-zero, wavenumber. Consequently, the late-time behaviour $t > t_{on}$ of these systems cannot be modelled by methods that expand about a dominant mode. This behaviour may arise because no single wavenumber dominates within the linear regime. Rather, immediately prior to onset of nonlinear convection, there is a band of unstable wavenumbers with large growth rates.

The regular asymptotic expansion we propose opens the door to several avenues of promising future work. The expansion can be easily extended to include the effects of anisotropy and vertical heterogeneity. It can also be coupled with the optimization method of Daniel *et al.* (2013) to determine optimal initial perturbation profiles, $c_p(z)$, that minimize the onset time of nonlinear convection. Finally, we note that the application of the expansion to the case of continuously forced boundary layers is the topic of ongoing study.

Acknowledgements

The authors gratefully acknowledge helpful discussions with Don Daniel and Professor Balakumar Balachandran from the University of Maryland, College Park, and with Dr Denis Martinand from the University of Aix-Marseille. Valuable guidance and suggestions were also provided by anonymous reviewers. This study was sponsored by a generous research grant from the Petroleum Institute, Abu Dhabi.

Appendix A. Accuracy of DNS

The spatial and temporal accuracies of the DNS method are verified with respect to the following artificial, but exact, analytical solution,

$$u_e = -\sin\left(\frac{2\pi a x}{L}\right)\cos(2\pi b z)\cos(\beta t), \quad w_e = \frac{a}{bL}\cos\left(\frac{2\pi a x}{L}\right)\sin(2\pi b z)\cos(\beta t), \tag{A 1}$$

$$c_e = \frac{1}{abL}(a^2 + b^2L^2)\cos\left(\frac{2\pi a x}{L}\right)\sin(2\pi b z)\cos(\beta t), \tag{A 2}$$

where $a = b = 16$ produce highly oscillatory test fields. Solution (A 1) and (A 2) satisfies (2.1) and (2.2) with the addition of a forcing term F to the right-hand-side

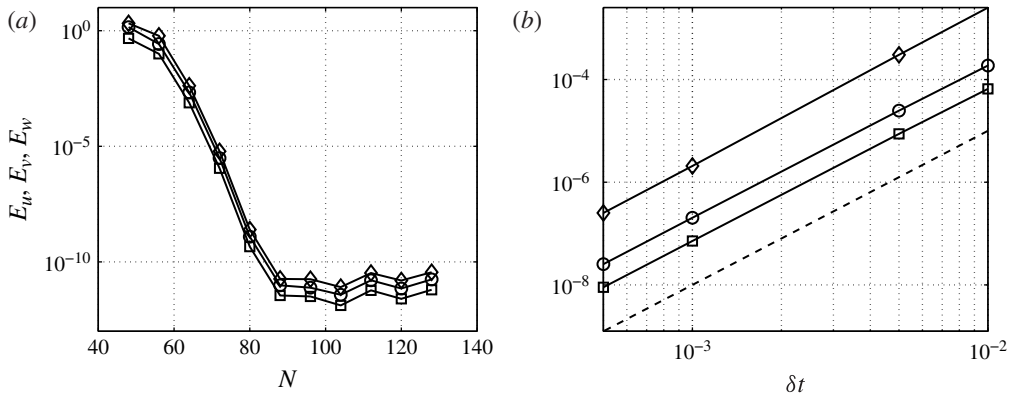

FIGURE 10. Spatial and temporal accuracy of the direct numerical method for $L = 2\pi$ and $Ra = 1$. (*a*) Plot of E_u (circles), E_w (squares) and E_c (diamonds) versus N for $\beta = 0$, $\mathrm{d}t = 0.0$. (*b*) Plot of E_u (circles), E_w (squares) and E_c (diamonds) versus δt for $\beta = 4$, $N = M = 128$. The dashed line illustrates a slope of δt^3.

of the advection–diffusion (3.14). The boundary conditions (3.16) are modified so that

$$w^{n+1}\Big|_{z=0,1} = w_e\Big|_{z=0,1}, \quad c^{n+1}\Big|_{z=0} = c_e\Big|_{z=0}, \quad \frac{\partial c^{n+1}}{\partial z}\Big|_{z=1} = \frac{\partial c_e}{\partial z}\Big|_{z=1}. \tag{A 3}$$

To test the spatial accuracy of the method, we set $\beta = 0$, $\mathrm{d}t = 0.01$, $N_x = N_z$, $c^0 = \boldsymbol{v}^0 = 0$ and integrate in time until steady state, after which we measure the error as $E_f = \|f - f_e\|_\infty$, where $f = u$, w or c and $f_e = u_e$, w_e or c_e. Figure 10(*a*) demonstrates the method converges spectrally to $E_f \sim \mathscr{O}(10^{-12})$. To test temporal accuracy, we set $\beta = 4$, $N = M = 128$, and $c^0 = c_e^0$, $\boldsymbol{v}^0 = \boldsymbol{v}_e^0$. The fields are integrated from $t = 0$ to $t = 1$ for $10^{-4} \leqslant \delta t \leqslant 10^{-2}$. Figure 10(*b*) confirms third-order temporal accuracy.

Appendix B. Comparison with RB convection

In this appendix, we present DNS of RB convection in a porous layer. These are useful for comparison with the results presented in § 5.1. For this purpose, we modify the boundary condition (2.2) so that

$$c\big|_{z=0} = 1, \quad c\big|_{z=1} = 0, \quad w\big|_{z=0} = w\big|_{z=1} = 0. \tag{B 1}$$

Equations (2.1) and (B 1) satisfy the steady base state $c_b(z) = 1 - z$. We perform a classical linear modal stability analysis (Drazin & Reid 1981) to obtain the neutral curve in the (k, Ra) plane illustrated in figure 11(*a*). The unstable region has been shaded grey. This region shows combinations of k and Ra for which there is at least one unstable eigenmode. The critical point $(k_c, Ra_c) = (3.06, 39.5)$ is marked with a solid dot.

The positive growth rates produced by RB convection are much smaller than those produced by the transient diffusive boundary layer considered in the current study. For $Ra \leqslant 60$, we observe that the maximum growth rates produced by RB convection are on the order of $\sigma \sim \mathscr{O}(0.1)$. In contrast, the diffusive boundary layer considered in the current study produces growth rates as large as $\sigma = 2$ when $Ra = 500$, (see Tilton *et al.* 2013, for details).

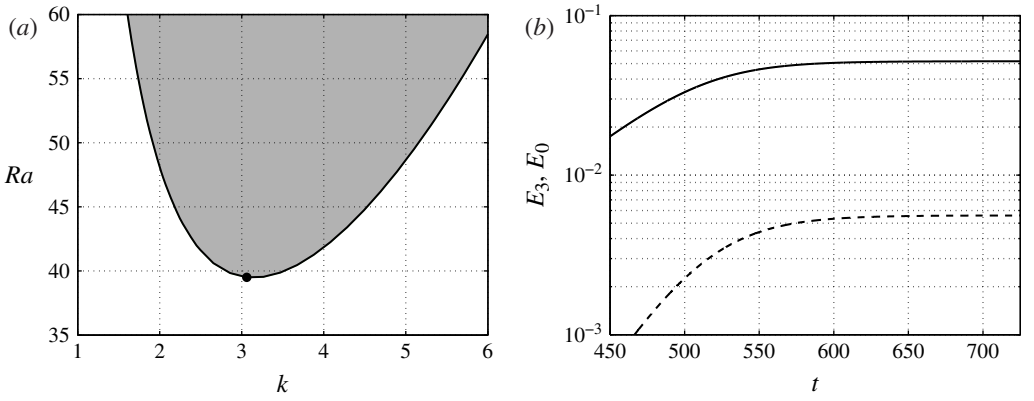

FIGURE 11. Results for RB convection. (*a*) Neutral curve (solid line) in the (k, Ra) plane. The unstable region is shaded grey. The solid dot marks the critical point $(k_c, Ra_c) = (3.06, 39.5)$. (*b*) DNS results for E_3 (solid line) and E_0 (dashed) line when the base state $c_b = 1 - z$ is perturbed at $t_p = 0$ with the dominant eigenmode for $k = 3$ and $Ra = 45$. Following an initial period of exponential growth, E_3 and E_0 plateau to constant values for which $E_0 \ll E_3$.

For comparison with the results presented in figure 5(*a*) of § 5.1, figure 11(*b*) shows DNS results for the temporal evolution of E_3 (solid line) and E_0 (dashed line) when the base state $c_b = 1 - z$ is perturbed with the dominant eigenmode for $k = 3$ and $Ra = 41$ at the initial time $t_p = 0$. Following a long period of exponential growth, $t < 450$, the magnitude of the fundamental, E_3, and the zero-wavenumber response, E_0, eventually plateau to constant values for which $E_0 \ll E_3$. In contrast, the results presented in figure 5(*a*) demonstrate that in the case of transient diffusive boundary layers, the magnitude of the zero-wavenumber response eventually surpasses that of the fundamental.

REFERENCES

BEN, Y., DEMEKHIN, E. A. & CHANG, H.-C. 2002 A spectral theory for small-amplitude miscible fingering. *Phys. Fluids* **14**, 999–1010.

BLAIR, L. M. & QUINN, J. A. 1969 The onset of convection in a fluid layer with time-dependent density gradients. *J. Fluid Mech.* **36**, 385–400.

BREUGEM, W. P. & BOERSMA, B. J. 2005 Direct numerical simulations of turbulent flow over a permeable wall using a direct and a continuum approach. *Phys. Fluids* **17**, 025103.

CALTAGIRONE, J. P. 1980 Stability of a saturated porous layer subject to a sudden rise in surface temperature: comparison between linear and energy methods. *Q. J. Mech. Appl. Maths.* **33**, 47–58.

CAMPOREALE, C., MANTELLI, E. & MANES, C. 2013 Interplay among unstable modes in films over permeable walls. *J. Fluid Mech.* **719**, 527–550.

DANIEL, D., TILTON, N. & RIAZ, A. 2013 Optimal perturbations of gravitationally unstable, transient boundary layers in porous media. *J. Fluid Mech.* **727**, 456–487.

DOUMENC, F., BOECK, T., GUERRIER, B. & ROSSI, M. 2010 Transient Rayleigh–Bénard–Marangoni convection due to evaporation: a linear non-normal stability analysis. *J. Fluid Mech.* **648**, 521–539.

DRAZIN, P. G. & REID, W. H. 1981 *Hydrodynamic Stability*. Cambridge University Press.

ELENIUS, M. T., NORDBOTTEN, J. M. & KALISCH, H. 2012 Effects of capillary transition on the stability of a diffusive boundary layer. *IMA J. Appl. Maths.* **77**, 771–787.

ENNIS-KING, J. & PATERSON, L. 2003 Role of convective mixing in the long-term storage of carbon dioxide in deep saline formations. *SPE* **10** (3), 349–356.

FOSTER, T. D. 1965 Stability of a homogeneous fluid cooled uniformly from above. *Phys. Fluids* **8**, 1249–1257.

GODRECHE, C. & MANNEVILLE, P. 1998 *Hydrodynamics and Nonlinear Instabilities*. Cambridge Univeristy Press.

GOLDSTEIN, A. W. 1959 Stability of a horizontal fluid layer with unsteady heating from below and time-dependent body force. *Tech. Rep.* R-4. NASA.

GREEN, L. L. & FOSTER, T. D. 1975 Secondary convection in a Hele Shaw cell. *J. Fluid Mech.* **71**, 675–687.

GRESHO, P. M. & SANI, R. L. 1971 The stability of a fluid layer subjected to a step change in temperature: transient vs. frozen time analyses. *Int. J. Heat Mass Transfer* **14**, 207–221.

HASSANZADEH, H., POOLADI-DARVISH, M. & KEITH, D. W. 2006 Stability of a fluid in a horizontal saturated porous layer: effect of non-linear concentration profile, initial, and boundary conditions. *Trans. Porous Med.* **65**, 193–211.

HEWITT, D. R., NEUFELD, J. A. & LISTER, J. R. 2013 Convective shutdown in a porous medium at high Rayleigh number. *J. Fluid Mech.* **719**, 551–586.

HIRATA, S. C., GOYEAU, B. & GOBIN, D. 2007 Stability of natural convection in superposed fluid and porous layers: influence of the interfacial jump boundary condition. *Phys. Fluids* **19**, 058102.

JAMES, D. F. & DAVIS, A. M. J. 2001 Flow at the interface of a model fibrous porous medium. *J. Fluid Mech.* **426**, 47–72.

JHAVERI, B. S. & HOMSY, G. M. 1982 The onset of convection in fluid layers heated rapidly in a time-dependent manner. *J. Fluid Mech.* **114**, 251–260.

JOSEPH, D. D. 1976 *Stability of Fluid Motions*. Springer.

KAVIANY, M. 1984 Onset of thermal convection in a saturated porous medium: experiment and analysis. *Int J. Heat Mass Transfer* **27**, 2101–2110.

KIM, M. C. & CHOI, C. K. 2012 Linear stability analysis on the onset of buoyancy-driven convection in liquid-saturated porous medium. *Phys. Fluids* **24**, 044102.

KIM, M. C. & KIM, S. 2005 Onset of convective instability in a fluid-saturated porous layer subject to time-depedent heating. *Intl. Commun. Heat Mass Transfer* **32**, 416–424.

LICK, W. 1965 The instability of a fluid layer with time-dependent heating. *J. Fluid Mech.* **21**, 565–576.

MALKUS, W. V. R. & VERONIS, G. 1958 Finite amplitude cellular convection. *J. Fluid Mech.* **4**, 225–260.

MORTON, B. R. 1957 On the equilibrium of a stratified layer of a fluid. *J. Mech. Appl. Math.* **10**, 433–447.

NAYFEH, A. H. 1981 *Introduction to Perturbation Techniques*. John Wiley and Sons.

ORR, F. M. 2009 Onshore geologic storage of CO_2. *Science* **325**, 1656–1658.

PALM, E. 1960 On the tendency towards hexagonal cells in steady convection. *J. Fluid Mech.* **8**, 183–192.

PAU, G. S. H., BELL, J. B., PRUESS, K., ALMGREN, A. S., LIJEWSKI, M. J. & ZHANG, K. 2010 High-resolution simulation and characterization of density-driven flow in CO_2 storage in saline aquifers. *Adv. Water Resour.* **33**, 443–455.

PEYRET, R. 2002 *Spectral Methods for Incompressible Viscous Flows*. Springer-Verlag.

PRITCHARD, D. 2004 The instability of thermal and fluid fronts during radial injection in a porous medium. *J. Fluid Mech.* **508**, 133–163.

RAPAKA, S., CHEN, S., PAWAR, R. J., STAUFFER, P. H. & ZHANG, D. 2008 Non-modal growth of perturbations in density-driven convection in porous media. *J. Fluid Mech.* **609**, 285–303.

REES, D. A. S., SELIM, A. & ENNIS-KING, J. P. 2008 The instability of unsteady boundary layers in porous media. In *Emerging Topics in Heat and Mass Transfer in Porous Media* (ed. P. Vadász), pp. 85–110. Springer.

RIAZ, A., HESSE, M., TCHELEPI, A. & ORR, F. M. 2006 Onset of convection in a gravitationally unstable diffusive boundary layer in porous media. *J. Fluid Mech.* **548**, 87–111.

ROBINSON, J. L. 1976 Theoretical analysis of convective instability of a growing horizontal thermal boundary layer. *Phys. Fluids* **19**, 778–791.

SLIM, A. C., BANDI, M. M., MILLER, J. C. & MAHADEVAN, L. 2013 Dissolution-driven convection in a Hele-Shaw cell. *Phys. Fluids* **25**, 024101.

SLIM, A. C. & RAMAKRISHNAN, T. S. 2010 Onset and cessation of time-dependent, dissolution-driven convection in porous media. *Phys. Fluids* **22**, 124103.

SPANGENBERG, W. G. & ROWLAND, W. R. 1961 Convective circulation in water induced by evaporation. *Phys. Fluids* **4**, 743–750.

SPARROW, E. M., BEAVERS, G. S., CHEN, T. S. & LLOYD, J. R. 1973 Breakdown of the laminar flow regime in permeable-walled ducts. *J. Appl. Mech.* **40**, 337–342.

TILTON, N. & CORTELEZZI, L. 2008 Linear stability analysis of pressure-driven flows in channels with porous walls. *J. Fluid Mech.* **604**, 411–445.

TILTON, N., DANIEL, D. & RIAZ, A. 2013 The initial transient period of gravitationally unstable diffusive boundary layers developing in porous media. *Phys. Fluids* **25**, 092107.

WHITAKER, S. 1986 Flow in porous media I: a theoretical derivation of Darcy's law. *Trans. Porous Media* **1**, 3–25.

WHITAKER, S. 1999 *The Method of Volume Averaging*. Klumer Academic Publishers.

WOODING, R. A., TYLERS, S. W. & WHITE, I. 1997 Convection in groundwater below an evaporating salt lake: 1. Onset of instability. *Water Resour. Res.* **33**, 1199–1217.